



Atacama Large Millimeter / submillimeter Array

ALMA Cross Correlation Bandpass Stability

ALMA Technical Note Number: 15

Status: DRAFT

Prepared by:	Organization:	Date:
Seiji Kamenno (ALMA System Verification Scientist)	JAO/NAOJ	17 December 2014

ALMA Cross Correlation Bandpass Stability (Draft)

Seiji Kameno

December 17, 2014

This report addresses the cross-correlation bandpass stability of ALMA at Band 3, 4, 6, 7, 8, 9, and 10.

Aims. Verify present performance of cross-correlation bandpass stability which is critical for observations that require high spectral dynamic range. Then, identify origins of the bandpass instability and quest for solutions to mediate them.

Methods. Bright continuum point-like sources were observed with 21–35 antennas for longer than 1.5 hours. Antenna-based bandpass shape were determined in two methods: real–imaginary and amplitude–phase solutions. The bandpass variation was evaluated in terms of amplitude and phase by comparing the reference BP table. Linear regression was applied to find the control parameters to explain the bandpass variation. The bandpass flatness was measured by taking the spectral Allan variance.

Results. The real–imaginary solution showed better accuracy than the amplitude–phase solution. The bandpass stability was partially compliant at Band 3, 4, and 6, while the signal-to-noise ratio at Band 7 or higher was not sufficient to achieve the accuracy of 0.1% that is necessary to verify the requirement. We found that the bandpass variation was dominated by the random noise component and constant intercept, with weak dependence of atmospheric component. Time stability was sufficient for the timescale of ~ 1 day. The bandpass shape after bandpass calibration in TDM was flat enough in the frequency scale of $\Delta\nu < 125$ MHz. The bandpass shapes of TDM and FDM were different by ~ 2 %.

Conclusions. We got practical performance of cross-correlation bandpass stability at all working frequency bands. It is possible to predict the standard deviation of bandpass amplitude variation, $\Delta|B|$ as $\Delta|B| \sim a_0 + a_1 S$, where a_0 is the intercept depending on frequency bands and a_1 is the proportional coefficient on the random noise, S , given as $S^2 = \frac{1}{(N_{\text{ant,BP}} - 2)|V_{\text{BP}}|^2 \Delta\nu T_{\text{BP}}} + \frac{1}{(N_{\text{ant,tg}} - 2)|V_{\text{tg}}|^2 \Delta\nu T_{\text{tg}}}$. See subsection 5.1 for detail values of the parameters.

1 Introduction

The [draft System Verification report on the SYS273.2 cross correlation bandpass stability](#) was issued covering frequency bands of Band 3, 6, 7, and 9 with 15 – 21 antennas. The results did not verify the required accuracy of -30 dB because of insufficient signal-to-noise ratio.

The bandpass stability campaign in 2013 Oct – Nov and the high frequency campaign in 2014 May – Sep covered frequency bands of Band 3, 4, 6, 7, 8, 9, and 10 with 21–35 antennas. We attempted to retake the verification of cross-correlation bandpass stability using the datasets taken in the campaigns.

1.1 Requirements

The requirement for the bandpass stability is defined as Req#273.2 in the ALMA System Technical Requirements ([ALMA-80.04.00.00-005-C-SPE](#)):

Bandpass Stability: spectral gain vrs time (T)	The 1 hr: Temporal change in bandpass gain or shape of cross correlation < -30 dB over 3600 seconds.
--	--

The requirement of 1000:1 is defined for looking for weak lines in presence of strong continuum emission. Further description on the requirement states:

Case (b) determines the bandpass stability for interferometric observations. The stability of the continuum within the passband has to be adequate and over long timescales. Assume that a bandpass calibration is done every 60 minutes and that spectra are sufficiently over-sampled that ringing is not a problem and that thermal noise is not significant. Then thermal changes which alter reflections and/or bandpass ripple in the analogue system may limit the spectral dynamic range. Therefore, the stability of the passband profile, with respect to the mean signal strength within the total IF, has to be better than -30 dB for a time of ~ 3600 seconds at a resolution bandwidth of 2 MHz.

1.2 Conditions for the Requirements

1. A strong point-like unpolarized continuum source that has a flat spectrum should be observed for the verification of bandpass characteristics. An ideal source yields constant visibilities so that the observed visibilities response only the complex gain of the observing system.
2. To evaluate the bandpass gain or shape, random (thermal) noise should be reduced as far as possible.
3. Complex (amplitude and phase) gain calibration should be employed before time integration of visibilities to avoid coherence loss. This treatment doesn't affect the bandpass shape because the applied complex gain is uniform across the band. The calibration includes residual-delay compensation that yields linear slope of phase across the band.
4. Band edges are excluded from the evaluation. In this report we trimmed 5% bandwidth off at band edges.
5. To evaluate antenna-based gain stability, solution for them is applied using the baseline-based visibilities. This improves the accuracy in determination of bandpass shape.
6. To evaluate the stability of the passband profile with respect to the mean signal strength, we employed the standard deviation (SD) defined as $\sqrt{\langle (B_k - \bar{B})^2 \rangle}$ and the peak excess

(PE) defined as $\max(|B_k - \bar{B}|)$ as the index of bandpass variation. Here, B_k is the bandpass amplitude at the k -th spectral channel and \bar{B} is the mean across the bandwidth. PE is used for judgement of compliant/non-compliant referring the system technical requirements, while SD is used for further statistical analysis such as p

2 Methods of Measurements

The model to describe complex visibility, $\mathbf{V}_{m,n}(t, \nu)$, of the baseline consisting of antenna m and n at the frequency, ν , and time, t , is:

$$\mathbf{V}_{ab}(t, \nu) = \mathbf{G}_a(t) \mathbf{G}_b^*(t) \mathbf{B}_a(\nu) \mathbf{B}_b^*(\nu) S \exp(i2\pi\nu(\tau_a - \tau_b)). \quad (1)$$

Here, $\mathbf{G}(t)$ is the antenna-based complex gain, $\mathbf{B}(\nu)$ is the antenna-based bandpass, S is the flux density of a flat-spectrum point source, and τ is the delay.

Since \mathbf{G} and \mathbf{B} are coupled, we can set $\bar{B} = 1$ and ascribe time variation of channel-averaged amplitude and phase to \mathbf{G} . Time variation of \mathbf{B} indicates the temporal change in bandpass shape that is described in the System Technical Requirements.

2.1 Antenna-Based Solutions

To determine the antenna-based bandpass using the baseline-based visibilities, we tried two solutions and compared their performances. The following subsections of 2.1.1 and 2.1.2 state solutions for \mathbf{G} and the same arguments are applicable to determine \mathbf{B} .

2.1.1 Amplitude-Phase Solutions

This method solved for amplitudes and phases independently. The visibility amplitude is proportional to the multiplication of antenna-based gain amplitudes. Taking logarithm of them, we have a linear equation between them. The visibility phase is the difference of antenna-based gain phase. Thus, we can employ a linear equation to solve them, too.

Let us formulate the equations with the visibilities \mathbf{V} and the antenna-based gain \mathbf{G}

$$\log |\mathbf{V}| = \begin{pmatrix} \log |\mathbf{V}_{1,0}| \\ \log |\mathbf{V}_{2,0}| \\ \log |\mathbf{V}_{2,1}| \\ \log |\mathbf{V}_{3,0}| \\ \log |\mathbf{V}_{3,1}| \\ \log |\mathbf{V}_{3,2}| \\ \vdots \end{pmatrix}, \quad \arg \mathbf{V} = \begin{pmatrix} \arg |\mathbf{V}_{1,0}| \\ \arg |\mathbf{V}_{2,0}| \\ \arg |\mathbf{V}_{2,1}| \\ \arg |\mathbf{V}_{3,0}| \\ \arg |\mathbf{V}_{3,1}| \\ \arg |\mathbf{V}_{3,2}| \\ \vdots \end{pmatrix} \quad (2)$$

$$\log |\mathbf{G}| = \begin{pmatrix} \log |\mathbf{G}_0| \\ \log |\mathbf{G}_1| \\ \log |\mathbf{G}_2| \\ \log |\mathbf{G}_3| \\ \vdots \end{pmatrix}, \quad \arg \mathbf{G} = \begin{pmatrix} \arg \mathbf{G}_1 \\ \arg \mathbf{G}_2 \\ \arg \mathbf{G}_3 \\ \vdots \end{pmatrix} \quad (3)$$

and the matrices

$$P_{\text{amp}} = \begin{pmatrix} 1 & 1 & 0 & 0 & 0 & \dots \\ 1 & 0 & 1 & 0 & 0 & \dots \\ 0 & 1 & 1 & 0 & 0 & \dots \\ 1 & 0 & 0 & 1 & 0 & \dots \\ 0 & 1 & 0 & 1 & 0 & \dots \\ 0 & 0 & 1 & 1 & 0 & \dots \\ \vdots & \vdots & \vdots & \vdots & \vdots & \ddots \end{pmatrix} \quad P_{\text{phs}} = \begin{pmatrix} 1 & 0 & 0 & 0 & \dots \\ 0 & 1 & 0 & 0 & \dots \\ -1 & 1 & 0 & 0 & \dots \\ 0 & 0 & 1 & 0 & \dots \\ -1 & 0 & 1 & 0 & \dots \\ 0 & -1 & 1 & 0 & \dots \\ \vdots & \vdots & \vdots & \vdots & \ddots \end{pmatrix} \quad (4)$$

as

$$\begin{aligned} W \log |\mathbf{V}| &= WP_{\text{amp}} \log |\mathbf{G}| \\ W \arg \mathbf{V} &= WP_{\text{phs}} \arg \mathbf{G}, \end{aligned} \quad (5)$$

where $W = \text{diag}(1/\sigma_{\text{vis}}^2)$ is the diagonal weighting matrix. The least-squares solution for equation 5 is given as

$$\begin{aligned} \log |\mathbf{G}| &= (P_{\text{amp}}^T W P_{\text{amp}})^{-1} W \log |\mathbf{V}| \\ \arg \mathbf{G} &= (P_{\text{phs}}^T W P_{\text{phs}})^{-1} W \arg \mathbf{V}. \end{aligned} \quad (6)$$

2.1.2 Real-Imaginary Solutions

\Re and \Im stand for real and imaginary parts of a complex variable, respectively. Since equation 1 involves multiplication of antenna-based complex gains, it is a non-linear equation. To solve it in real-imaginary form, we employ the iterative approach. Let the initial estimate of gain as $\hat{\mathbf{G}}$, the difference of the true gain, $\Delta \mathbf{G}$, and the visibility residual, $\Delta \mathbf{V}$ are defined as:

$$\Delta \mathbf{V} = \begin{pmatrix} \Re[\mathbf{V}_{1,0} - \hat{\mathbf{G}}_1 \hat{\mathbf{G}}_0^*] \\ \Re[\mathbf{V}_{2,0} - \hat{\mathbf{G}}_2 \hat{\mathbf{G}}_0^*] \\ \Re[\mathbf{V}_{2,1} - \hat{\mathbf{G}}_2 \hat{\mathbf{G}}_1^*] \\ \Re[\mathbf{V}_{3,0} - \hat{\mathbf{G}}_3 \hat{\mathbf{G}}_0^*] \\ \Re[\mathbf{V}_{3,1} - \hat{\mathbf{G}}_3 \hat{\mathbf{G}}_1^*] \\ \Re[\mathbf{V}_{3,2} - \hat{\mathbf{G}}_3 \hat{\mathbf{G}}_2^*] \\ \vdots \\ \Im[\mathbf{V}_{1,0} - \hat{\mathbf{G}}_1 \hat{\mathbf{G}}_0^*] \\ \Im[\mathbf{V}_{2,0} - \hat{\mathbf{G}}_2 \hat{\mathbf{G}}_0^*] \\ \Im[\mathbf{V}_{2,1} - \hat{\mathbf{G}}_2 \hat{\mathbf{G}}_1^*] \\ \Im[\mathbf{V}_{3,0} - \hat{\mathbf{G}}_3 \hat{\mathbf{G}}_0^*] \\ \Im[\mathbf{V}_{3,1} - \hat{\mathbf{G}}_3 \hat{\mathbf{G}}_1^*] \\ \Im[\mathbf{V}_{3,2} - \hat{\mathbf{G}}_3 \hat{\mathbf{G}}_2^*] \end{pmatrix}, \quad \Delta \mathbf{G} = \begin{pmatrix} \Re[\mathbf{G}_0 - \hat{\mathbf{G}}_0] \\ \Re[\mathbf{G}_1 - \hat{\mathbf{G}}_1] \\ \Re[\mathbf{G}_2 - \hat{\mathbf{G}}_2] \\ \Re[\mathbf{G}_3 - \hat{\mathbf{G}}_3] \\ \vdots \\ \Im[\mathbf{G}_1 - \hat{\mathbf{G}}_1] \\ \Im[\mathbf{G}_2 - \hat{\mathbf{G}}_2] \\ \Im[\mathbf{G}_3 - \hat{\mathbf{G}}_3] \end{pmatrix}. \quad (7)$$

Then, set the derivative matrix as:

$$P = \begin{pmatrix} \Re\hat{G}_1 & \Re\hat{G}_0 & 0 & 0 & 0 & \dots & & & & & \\ \Re\hat{G}_2 & 0 & \Re\hat{G}_0 & 0 & 0 & \dots & & & & & \\ 0 & \Re\hat{G}_2 & \Re\hat{G}_1 & 0 & 0 & \dots & \Im\hat{G}_2 & \Im\hat{G}_1 & 0 & \dots & \\ \Re\hat{G}_3 & 0 & 0 & \Re\hat{G}_0 & 0 & \dots & & & & & \\ 0 & \Re\hat{G}_3 & 0 & \Re\hat{G}_1 & 0 & \dots & \Im\hat{G}_3 & 0 & \Im\hat{G}_1 & 0 & \dots \\ 0 & 0 & \Re\hat{G}_3 & \Re\hat{G}_2 & 0 & \dots & 0 & \Im\hat{G}_3 & \Im\hat{G}_2 & 0 & \dots \\ & & & & \vdots & & & & & & \\ \Im\hat{G}_1 & 0 & 0 & 0 & 0 & \dots & \Re\hat{G}_0 & 0 & \dots & & \\ \Im\hat{G}_2 & 0 & 0 & 0 & 0 & \dots & 0 & \Re\hat{G}_0 & 0 & \dots & \\ 0 & \Im\hat{G}_2 & -\Im\hat{G}_1 & 0 & 0 & \dots & -\Re\hat{G}_2 & \Re\hat{G}_1 & 0 & \dots & \\ \Im\hat{G}_3 & 0 & 0 & 0 & 0 & \dots & 0 & 0 & \Re\hat{G}_0 & 0 & \dots \\ 0 & \Im\hat{G}_3 & 0 & -\Im\hat{G}_1 & 0 & \dots & -\Re\hat{G}_3 & 0 & \Re\hat{G}_1 & 0 & \dots \\ 0 & 0 & \Im\hat{G}_3 & -\Im\hat{G}_2 & 0 & \dots & 0 & -\Re\hat{G}_3 & \Re\hat{G}_2 & 0 & \dots \end{pmatrix}. \quad (8)$$

The equation of difference values will be

$$W\Delta V = WP\Delta G. \quad (9)$$

The solution of equation 9 is given as

$$\Delta G = (P^T W P)^{-1} W \Delta V \quad (10)$$

Then, the initial estimate of the gain will be modified as

$$\hat{G} \leftarrow \hat{G} + \Delta G. \quad (11)$$

By applying the iteration for a couple of cycles, the solution will converge to the neighborhood of the true value.

2.2 Evaluation of Time Stability

The time stability of bandpass shape is evaluated by comparing the antenna-based bandpass shapes between those at the reference epoch, $\mathbf{B}_0(\nu)$ and those at different epoch, $\mathbf{B}(t, \nu)$, in terms of amplitude and phase. Figure 1 shows the example. Upper and lower panels show bandpass amplitudes and phases, respectively. Blue lines and dots indicate the instantaneous antenna-based bandpass shape, while green lines and dots indicate the difference from the reference BP table. The differences of amplitude and phase are calculated as $\left| \frac{\mathbf{B}(t, \nu)}{\mathbf{B}_0(\nu)} \right| - 1$ and $\arg \frac{\mathbf{B}(t, \nu)}{\mathbf{B}_0(\nu)}$, respectively.

2.3 Spectral Allan Variance—Evaluation of Bandpass Flatness

The flatness of the bandpass shape was evaluated by the spectral Allan variance (SAV), $\sigma_y^2(\Delta\nu)$, defined as

$$\sigma_y^2(\Delta\nu) = \frac{\langle [B(\nu + \Delta\nu) - 2B(\nu) + B(\nu - \Delta\nu)]^2 \rangle}{2\Delta\nu^2}. \quad (12)$$

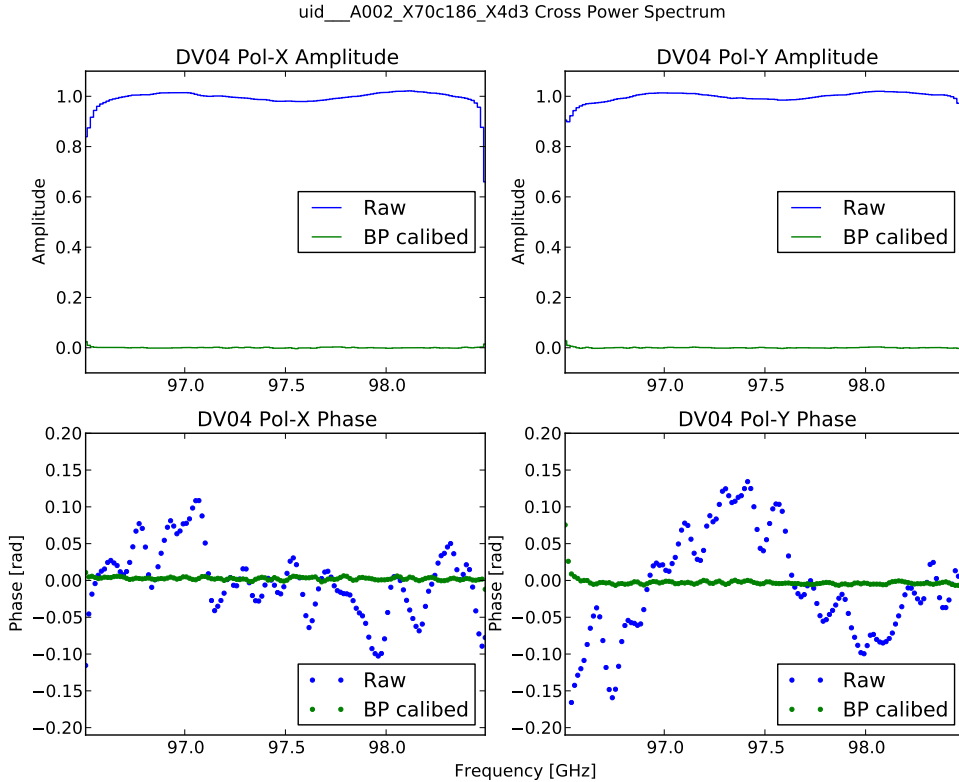


Figure 1: Cross power spectra of DV04 at Band-3. Top and bottom panels show the amplitudes and phases. Left and right panels stand for X and Y polarizations. Blue and green colors indicate the cross power spectra before and after bandpass calibration, respectively. The mean values of amplitude and phase are scaled to be unity and zero, respectively.

When bandpass variation is dominated by random thermal noise, we expect $\sigma_y^2 \propto \Delta\nu^{-2}$ because the numerator of equation 12 is independent on $\Delta\nu$. If the bandpass distortion is greater than the random thermal noise, we will have significant excess of SAV from the power law with the power index of -2 .

Figure 2 shows an example. After bandpass calibration was applied, the BP residual became flat and thus the SAV follows the power law with the power index of -2 . Note that the SAV at $\delta\nu = 1$ ch was underestimated because of Hanning-window apodization in the correlator.

3 Observations

Table 1 lists the observation log used in this report. Observations consisted of 1.5-hour SBEXs. Each SBEX consisted of 60 – 480 sec tracking scans toward a bright continuum source. Observations at Band 3, 6, 7, and 9 spread longer than one day inserted changes of frequency setups, while Band 4, 8, and 10 covers time range shorter than one day. Number of antennas are listed in the fourth column with the number of antennas unflagged in the parentheses. The asterisks marked with the source name indicates the bandpass calibration scan.

Table 1: List of observations

Band	uid://A002/	Date and Time (UT)	# Ants	Sources
3	X70c186/X168	2013/10/29 02:33 - 04:03	29 (27)	J042315-012034, J0522-364*, J0538-440
3	X70c186/X4d3	2013/10/29 04:10 - 05:40	29 (28)	J042315-012034, J0522-364, J0538-440
3	X70c186/X8b8	2013/10/29 05:45 - 07:16	29 (28)	J042315-012034, J0522-364, J0538-440
3	X70c186/X1091	2013/10/29 09:00 - 10:31	29 (28)	J042315-012034, J0522-364, J0538-440
3	X70f4b6/X39	2013/10/30 04:22 - 05:52	21 (20)	J042315-012034, J0522-364, J0538-440
3	X70f4b6/X4e4	2013/10/30 05:56 - 07:27	21 (20)	J042315-012034, J0522-364, J0538-440
3	X70f4b6/X9da	2013/10/30 07:31 - 08:34	21 (20)	J042315-012034, J0522-364, J0538-440
3	X73d9ce/X1ba	2013/11/24 04:44 - 06:15	32 (32)	J042315-012034, J0522-364, J0538-440
4	X89d540/X2ee	2014/08/22 05:13 - 06:48	30 (29)	3C 454.3*, J2232+117, J1924-292
6	X73a7bb/X3b9	2013/11/23 01:23 - 02:29	33 (33)	J042315-012034, J0522-364, J0538-440
6	X740d04/X4e5	2013/11/26 00:14 - 01:42	30 (29)	J042315-012034, J0522-364, J0538-440
6	X740d04/X7f7	2013/11/26 01:48 - 03:16	30 (30)	J042315-012034, J0522-364, J0538-440
6	X740d04/Xa57	2013/11/26 03:19 - 04:47	30 (30)	J042315-012034, J0522-364*, J0538-440
7	X812f8d/X1057	2014/05/09 10:51 - 11:29	21 (21)	J1924-292, 3C454.3*
7	X812f8d/X11bb	2014/05/09 11:37 - 12:15	21 (21)	J1924-292, 3C454.3
7	X8161ed/X1936	2014/05/11 10:26 - 11:58	21 (21)	3C 454.3, J2232+117, J1924-292
8	X8867ff/X1fbf	2014/08/02 12:23 - 13:55	26 (24)	J0522-364*, J0538-4405, J0510+1800
9	X8666c7/X1fa	2014/07/10 07:45 - 09:15	32 (32)	3C 454.4*
9	X8a2c58/Xb0	2014/08/26 06:42 - 08:16	35 (34)	3C 454.3
10	X8b8415/X5d7	2014/09/11 03:33 - 05:06	21 (21)	3C454.3*, J1924-292

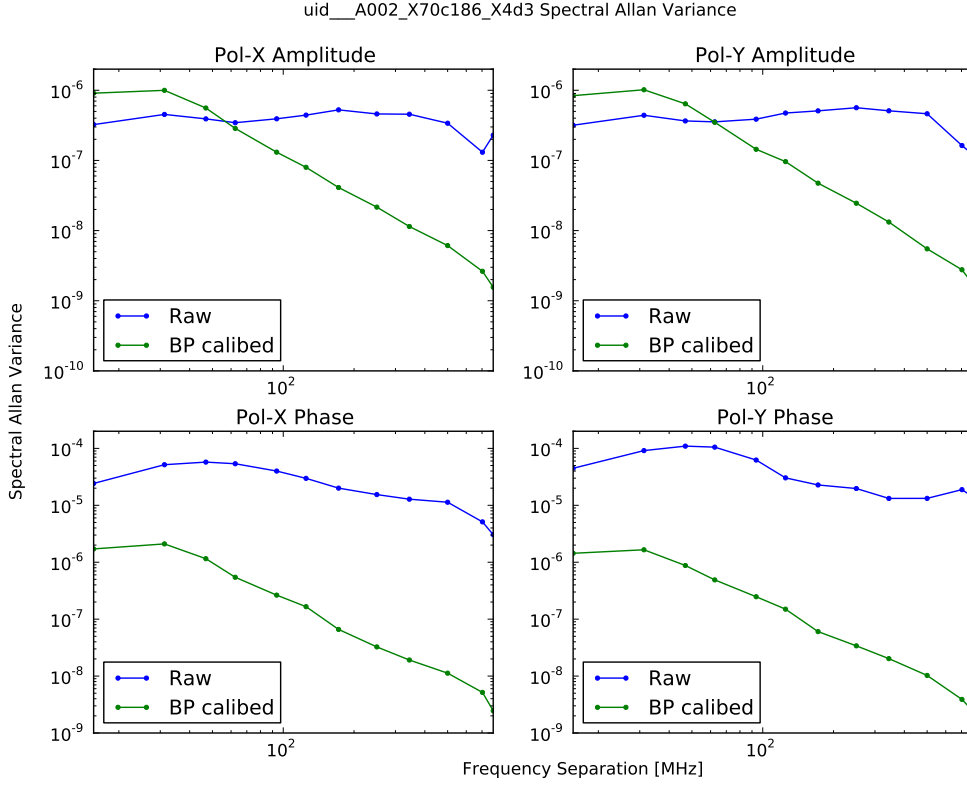


Figure 2: The spectral Allan variances (SAVs) of amplitude (top panel) and phase (bottom panel) as a function of frequency separation. Median values of the SAVs among 27 antennas are plotted.

4 Results

The performances of amplitude-phase and real-imaginary solutions are compared in subsection 4.1. While time stability was evaluated in TDM for all of frequency bands in subsection 4.2. The SAV was obtained to check spectral flatness of bandpass shape in subsection 4.3. FDM time stability was investigated in only at Band 4 in subsection 4.4 to test the performance of the TDM-to-FDM bandpass transfer method.

4.1 Amplitude-Phase versus Real-Imaginary Solutions

The comparison test of two solution methods, amplitude-phase and real-imaginary, was taken using the Band-7 observation toward J2232+117 using the narrow-band SPW in the FDM mode (234.375 MHz / 3840 ch, 61-kHz channel spacing). Figure 3 compares the solutions of the two methods, indicating better accuracy by the real-imaginary method than by the amplitude-phase. The standard deviation of amplitude and phase were 15.03% and 0.1820 rad by real-imaginary solution, while amplitude-phase method resulted in 15.08% and 0.1822 rad. We employed the real-imaginary method after this.

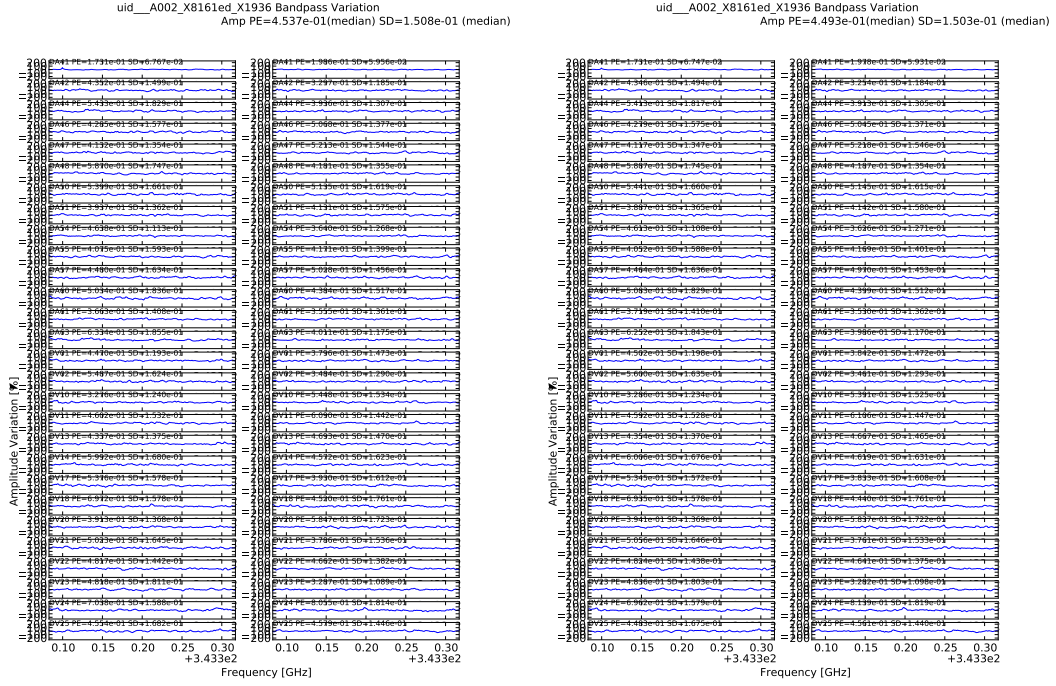
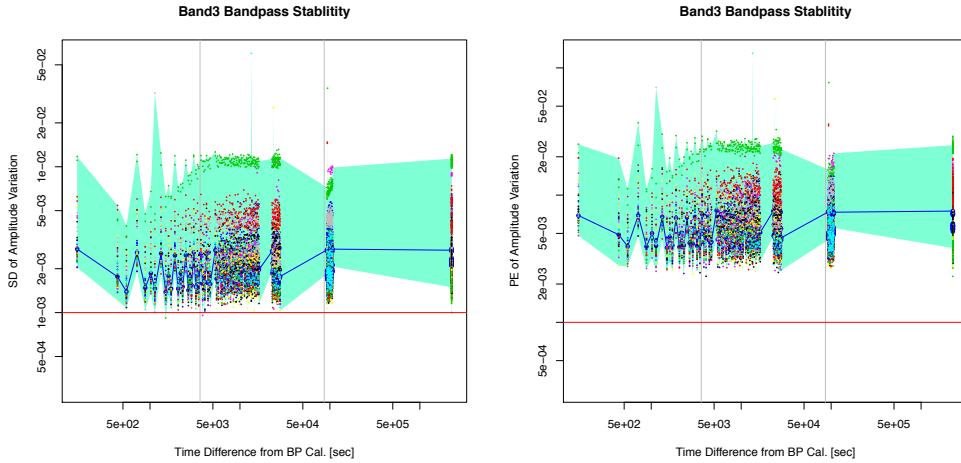


Figure 3: Comparison of amplitude-phase (left) and real-imaginary (right) solutions for antenna-based bandpass. The test was carried out using the Band-7 observations toward J2232 + 117 with 28 12-m antennas. The cross power spectra over 234.375 MHz / 3840 ch (61-kHz channel spacing) was smoothed with `Rbf(smooth=0.1)` for the reference bandpass and with `Rbf(smooth=0.05)` for the target spectrum. The relative amplitude variations of the cross power spectrum with respect to the reference bandpass are shown in each antenna and polarization panel.

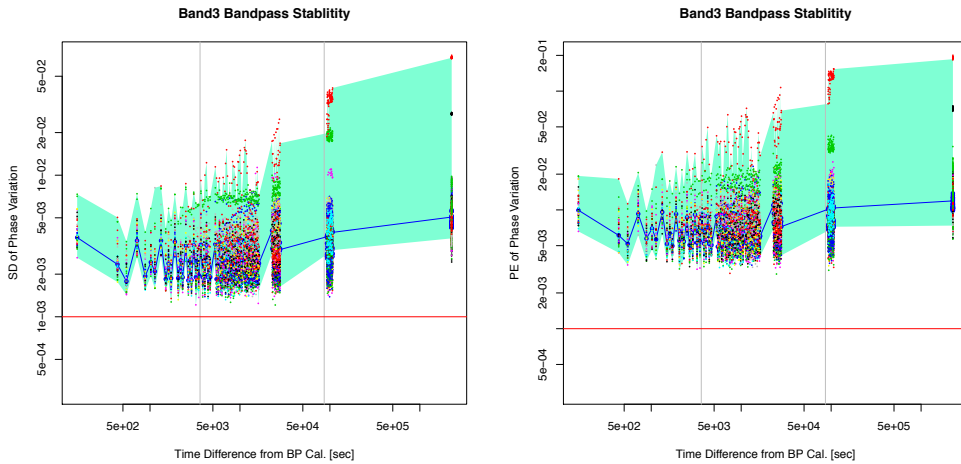
4.2 TDM Bandpass Variations

The time series plots of antenna-based bandpass variations are archived in [JIRA CSV-2964](#). Figures 4 – 10 shows the bandpass variations as a function of elapsed time since BP calibration scan. Four panels in each band stand for SD(amp), PE(amp), SD(phase), and PE(phase) as an indicator of bandpass variation as described in subsection 2.2.

Band 3



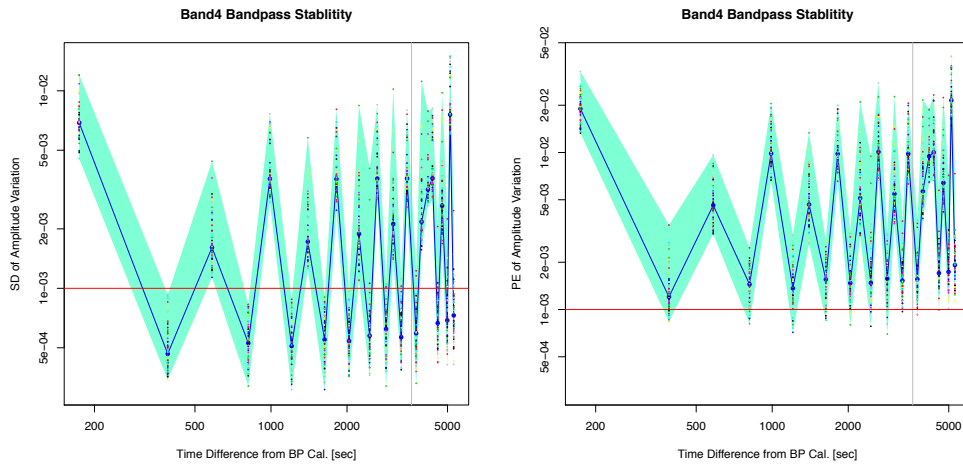
(a) SD (left) and PE (right) of bandpass amplitude variation at band 3 as a function of time difference between bandpass-calibration scans.



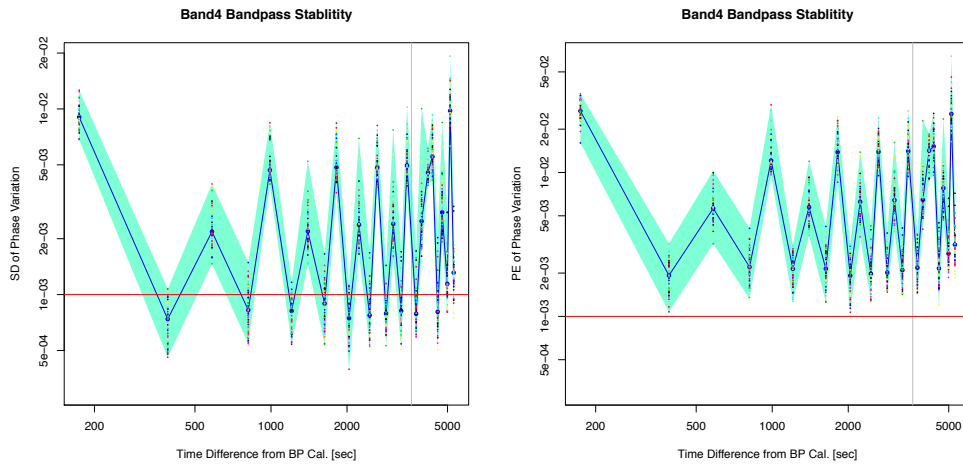
(b) SD (left) and PE (right) of bandpass phase variation at band 3

Figure 4: Band-3 bandpass variation. Small colored dots stand for antennas and polarizations. The mint filled area indicates the range of dots and the blue circles with solid lines indicate the median values. Two gray vertical lines point the timescales of 1 hour and 1 day, respectively. The red horizontal line indicates the required stability of -30 dB.

Band 4



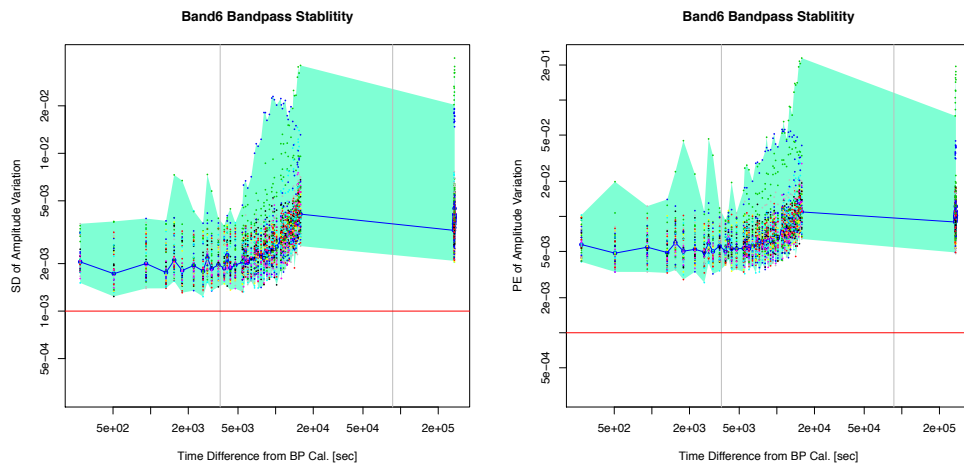
(a) SD (left) and PE (right) of bandpass amplitude variation at band 4.



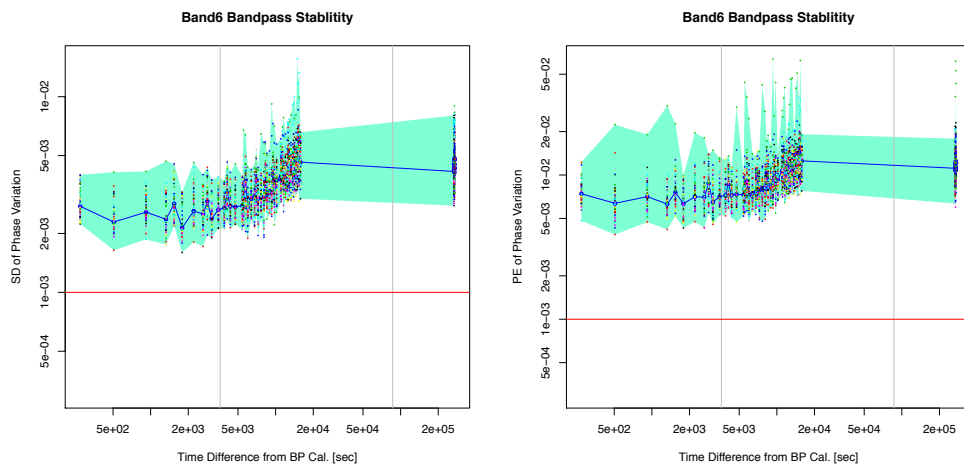
(b) SD (left) and PE (right) of bandpass phase variation at band 4

Figure 5: Band-4 bandpass variation. See figure 4 caption for the legend.

Band 6



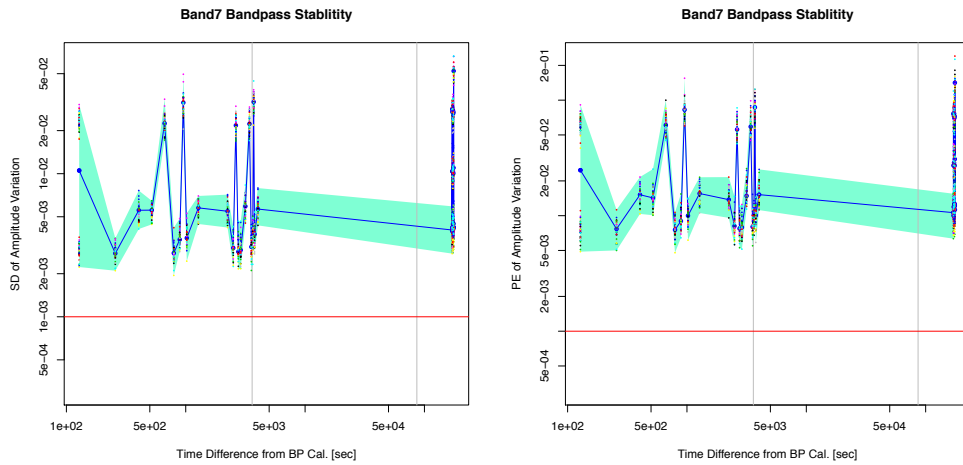
(a) SD (left) and PE (right) of bandpass amplitude variation at band 6.



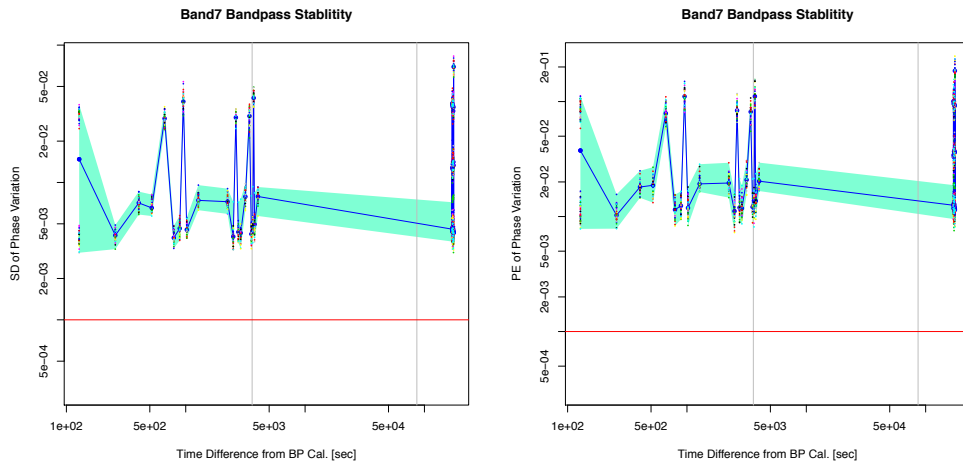
(b) SD (left) and PE (right) of bandpass phase variation at band 6.

Figure 6: Band-6 bandpass variation. See figure 4 caption for the legend.

Band 7



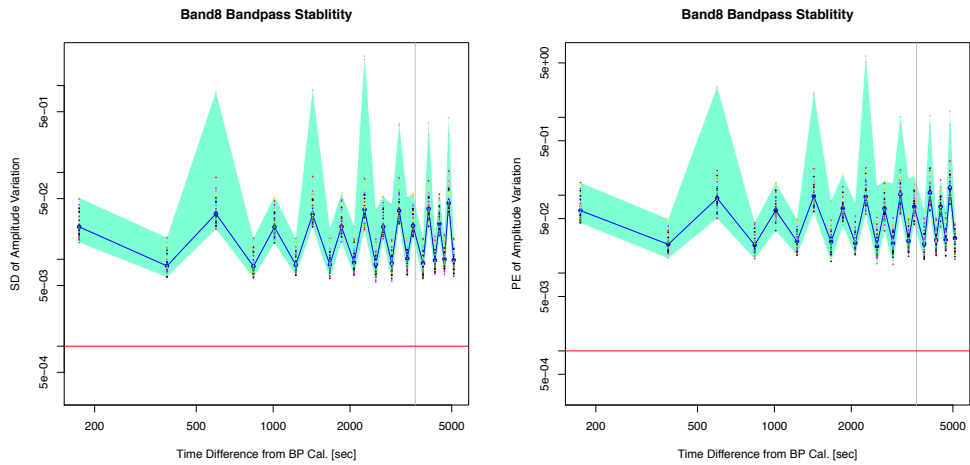
(a) SD (left) and PE (right) of bandpass amplitude variation at band 7.



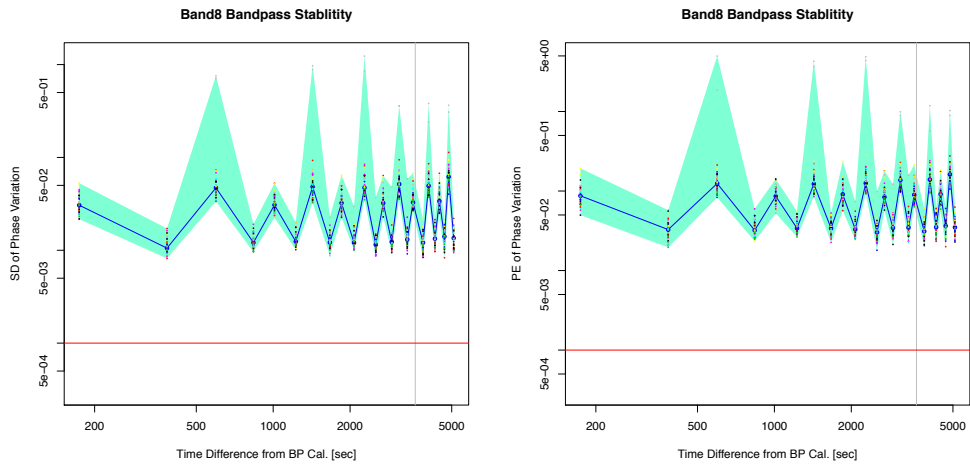
(b) SD (left) and PE (right) of bandpass phase variation at band 7.

Figure 7: Band-7 bandpass variation. See figure 4 caption for the legend.

Band 8



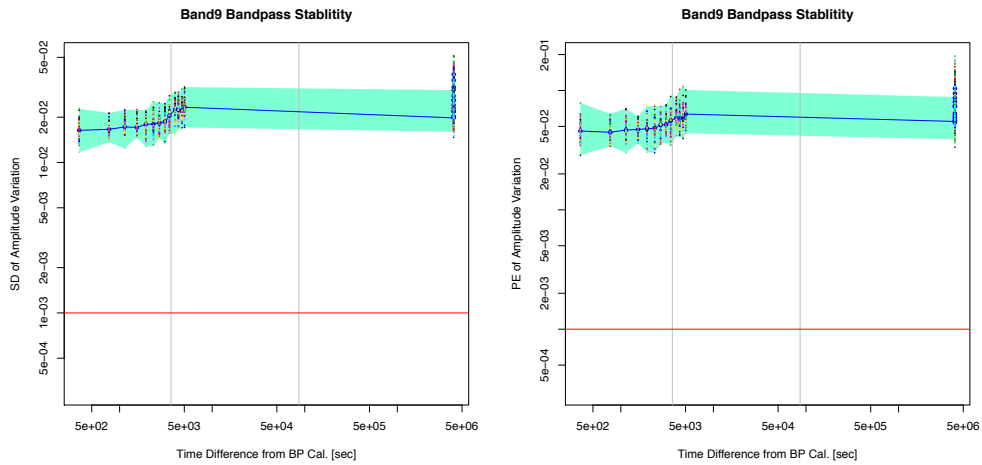
(a) SD (left) and PE (right) of bandpass amplitude variation at band 8.



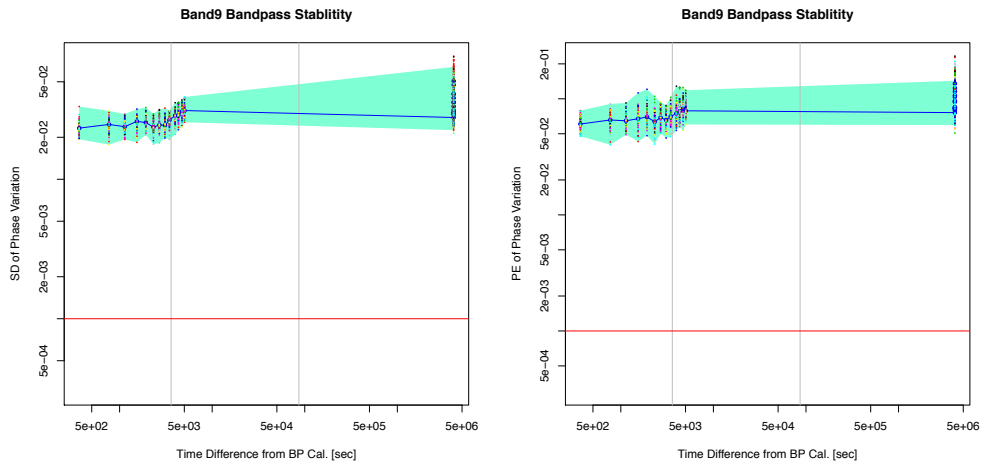
(b) SD (left) and PE (right) of bandpass phase variation at band 8.

Figure 8: Band-8 bandpass variation. See figure 4 caption for the legend.

Band 9



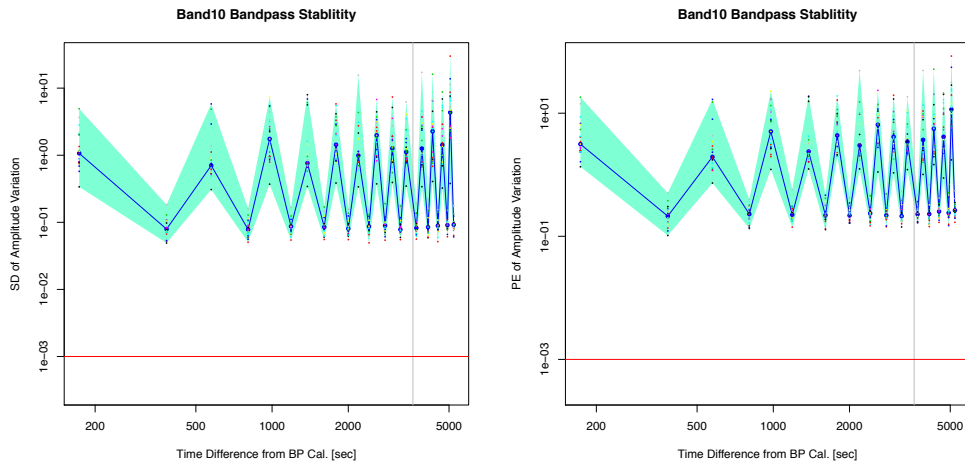
(a) SD (left) and PE (right) of bandpass amplitude variation at band 9.



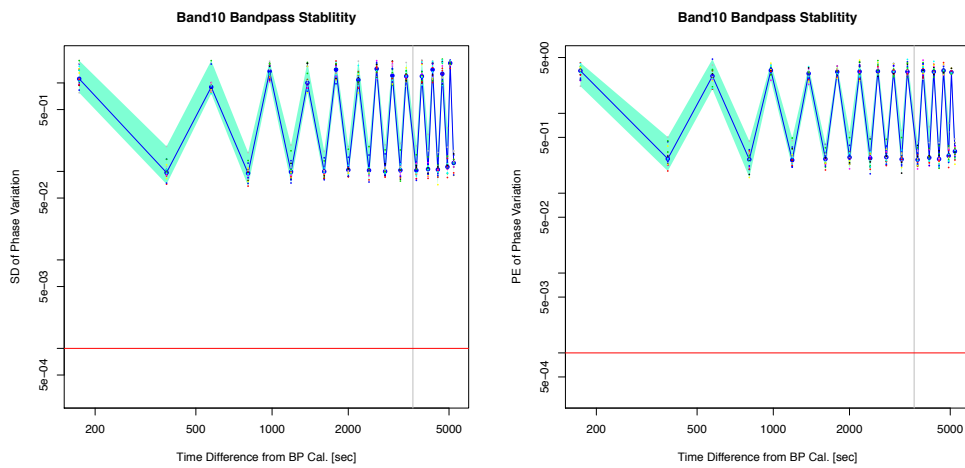
(b) SD (left) and PE (right) of bandpass phase variation at band 9.

Figure 9: Band-9 bandpass variation. See figure 4 caption for the legend.

Band 10



(a) SD (left) and PE (right) of bandpass amplitude variation at band 10.



(b) SD (left) and PE (right) of bandpass phase variation at band 10.

Figure 10: Band-10 bandpass variation. See figure 4 caption for the legend.

4.3 Spectral Allan Variance

SAVs are evaluated for the scans 1-hour later than the bandpass calibration scans toward the same source with the bandpass calibrator. We calculated each SAV of the antenna-based bandpass shape and took median values of SAVs among all antennas. The results are plotted in figures 11 – 17. The blue and green lines indicate SAVs before and after bandpass calibration. The red line guides the power-law with the power index of -2 , which indicates the ideal case where the bandpass shape were flat and the variation were dominated by random noise. Note that the SAV at $\Delta\nu = 15.6$ MHz (1 ch) is underestimated in every case because the spectral resolution is coarser than the channel separation due to the Hanning window in lag domain.

Band 3

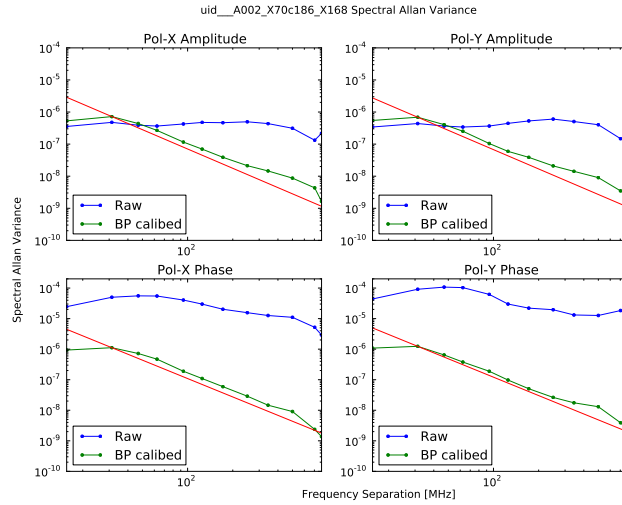


Figure 11: Band-3 spectral Allan variance

The non-flat spectral undulation significantly decreased through bandpass calibration. Both amplitude and phase SAVs after bandpass calibration follows the power law with the index of -2 in the frequency separation range of $32 \text{ MHz} < \Delta\nu < 125 \text{ MHz}$. The excess of amplitude SAV at $\Delta\nu > 250$ indicates bandpass shape variation at broad range of bandwidth.

Band 4

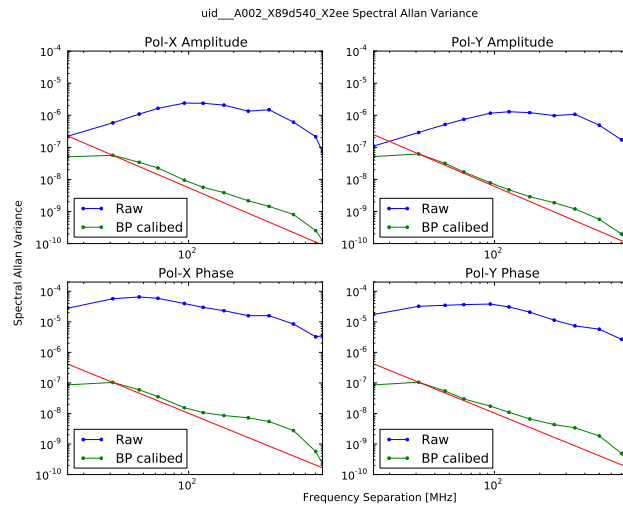


Figure 12: Band-4 spectral Allan variance

Behavior of the SAVs is similar to those at Band 3. The SAVs in $32 \text{ MHz} < \Delta\nu < 125 \text{ MHz}$ followed the power law with the index of -2 , which indicated that the bandpass variation is dominated by random white noise. Systematic variation of bandpass shape was significant at broad band range of $\Delta\nu > 125 \text{ MHz}$.

Band 6

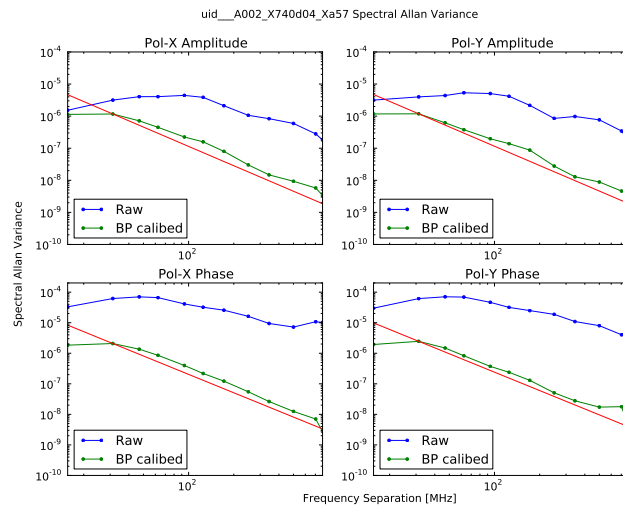


Figure 13: Band-6 spectral Allan variance

Bandpass calibration efficiently reduced the SAVs at all range of frequency separation. The SAVs after bandpass calibration showed a slight excess at $\Delta\nu > 125 \text{ MHz}$ with respect to the white noise component.

Band 7

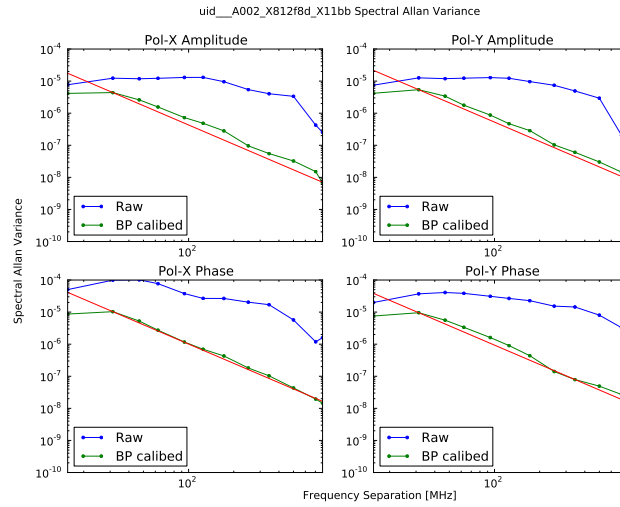


Figure 14: Band-7 spectral Allan variance

Bandpass calibration significantly reduced the SAV at all range of frequency separation. The SAVs after bandpass calibration followed the power-law with the power index of -2 . This indicates that the systematic variation of bandpass shape is hidden behind the white noise.

Band 8

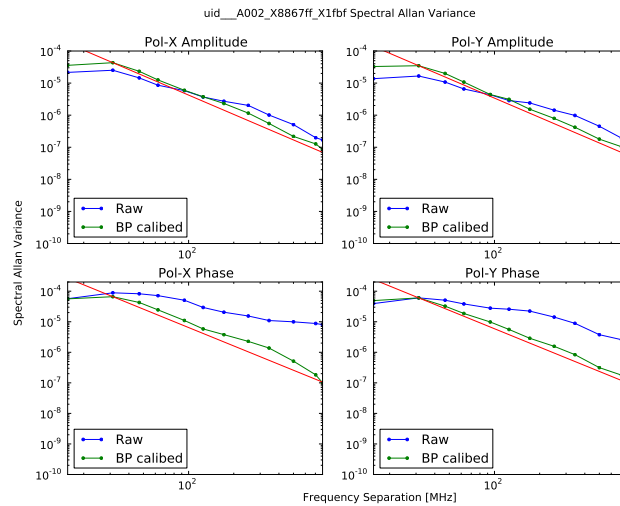


Figure 15: Band-8 spectral Allan variance

The effect of bandpass calibration was significant in bandpass phase at whole frequency separation range, and in amplitude at $\Delta\nu > 170$ MHz. This indicates that the amplitude undulation of the raw bandpass shape was comparable to the white noise.

Band 9

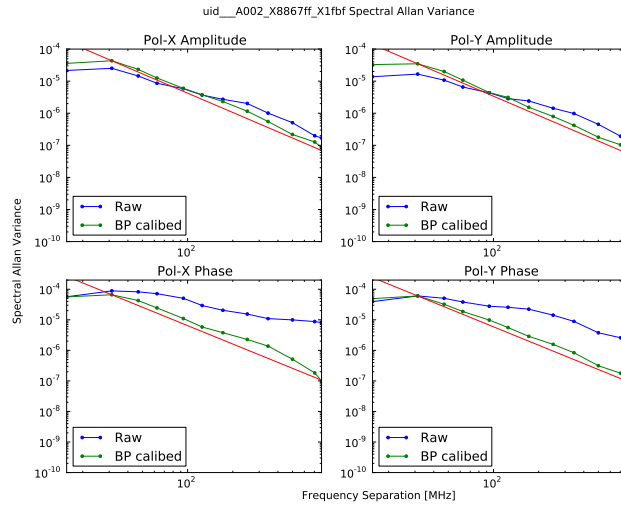


Figure 16: Band-9 spectral Allan variance

Similar behavior to that at Band 8. The effect of bandpass calibration in amplitude was limited at the frequency separation range of $\Delta\nu > 170$ MHz.

Band 10

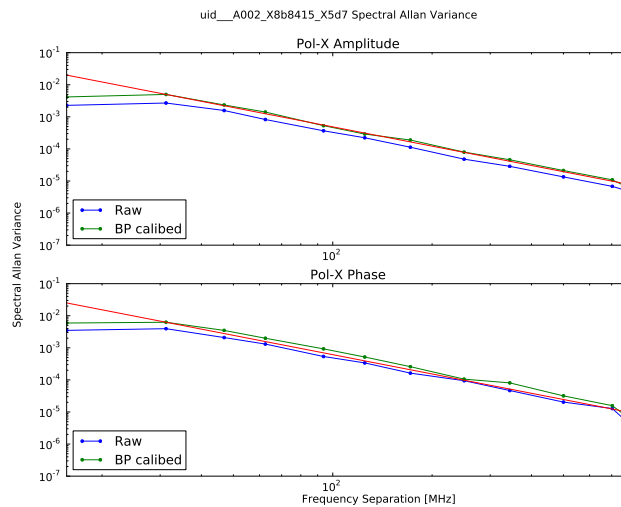


Figure 17: Band-10 spectral Allan variance

No significant effect through bandpass calibration. There was no significant undulation in amplitude of raw bandpass shape, compared with the random noise level. The SAVs after bandpass calibration were greater than those of raw bandpass shape in the whole frequency separation range. This indicates that the bandpass calibration at Band 10 was harmful rather than efficient for accuracy in spectral measurements.

4.4 FDM Bandpass Stability

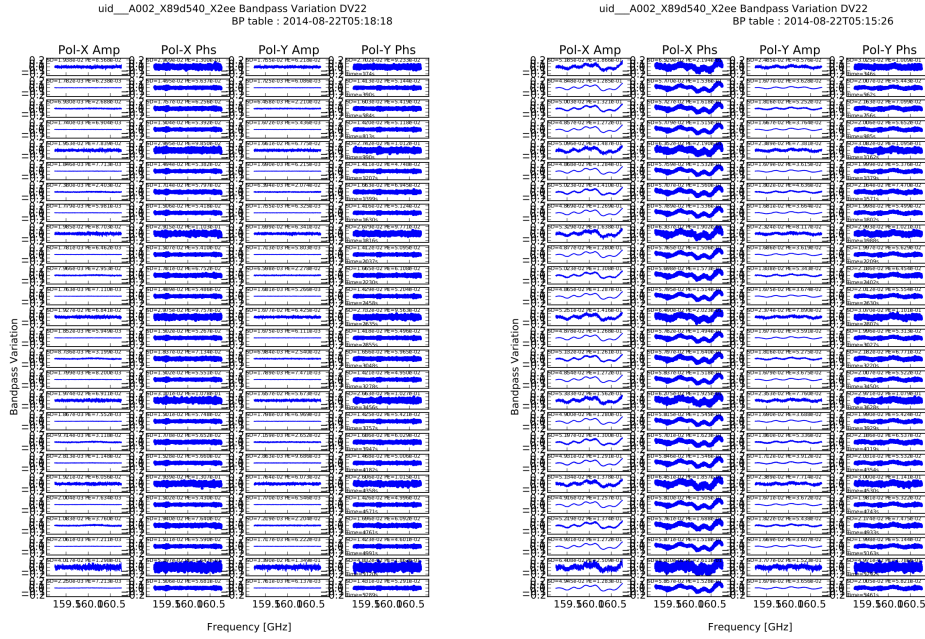


Figure 18: Comparison between FDM-FDM and TDM-FDM bandpass transfer. Bandpass variations at band 4 are plotted. (Left): Bandpass table was determined using the same FDM SPW. (Right): Bandpass table was produced in the TDM SPW and interpolated for FDM spectral channels.

The bandpass stability in the FDM mode was verified at Band 4 where the best performance of bandpass stability in the TDM mode was obtained. To evaluate the FDM bandpass stability, we tested two different BP tables generated from TDM and FDM SPWs. The TDM and FDM SPWs were tuned at the same center frequency, with the different bandwidths and the channel separations of (2000 MHz bandwidth / 128 ch) in TDM and (1875 MHz / 3840 ch) in FDM, respectively.

To realize the idea that TDM-based BP table (2 GHz bandwidth / 128 ch) to apply FDM SPWs, the TDM BP table was interpolated into the spectral resolution of FDM. The TDM BP table was smoothed and interpolated to accommodate the FDM SPW.

Figure 18 compares variations of spectral shape through FDM-BP and TDM-BP calibrations. While FDM-BP calibration resulted in flat spectral shape, significant systematic undulation appeared in TDM-BP calibration.

Figure 19 plots the SD values of amplitude as a function of elapsed time since the scan for the BP table. Although the residual in the FDM-to-FDM BP calibration was consistent with the TDM-to-FDM results (see figure 5), that in the TDM-to-FDM BP calibration was dominated by the systematic undulation and was less dependent on the signal-to-noise ratio.

Figure 20 show the SAVs of bandpass shape. The FDM-to-FDM bandpass calibration resulted in flat spectrum whose SAV is dominated by white noise. On the other hand, significant systematic undulation remained in TDM-to-FDM bandpass calibration that appeared the local peaks of SAV at $\Delta\nu = 125$ MHz and 7.8 MHz for amplitude and phase, respectively.

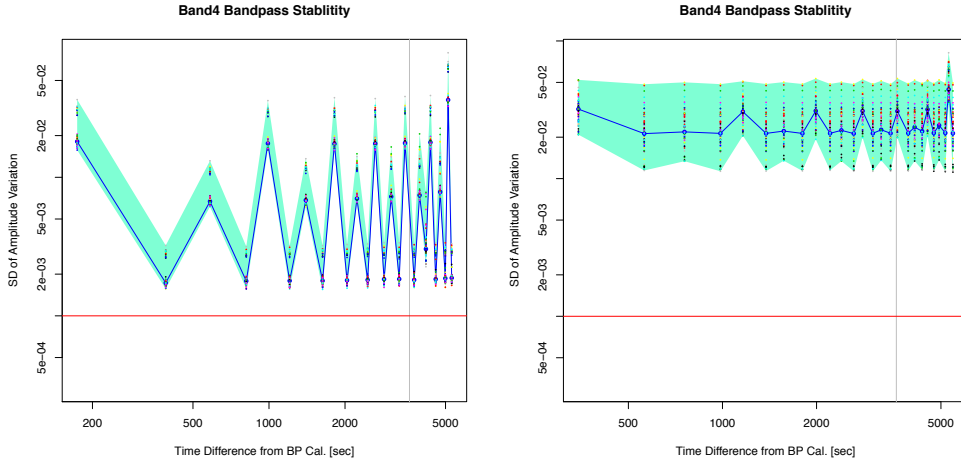


Figure 19: Time series of bandpass variation at band 4. Left and right panels stand for bandpass tables determined using FDM and TDM SPWs, respectively. See figure 4 caption for the legend.

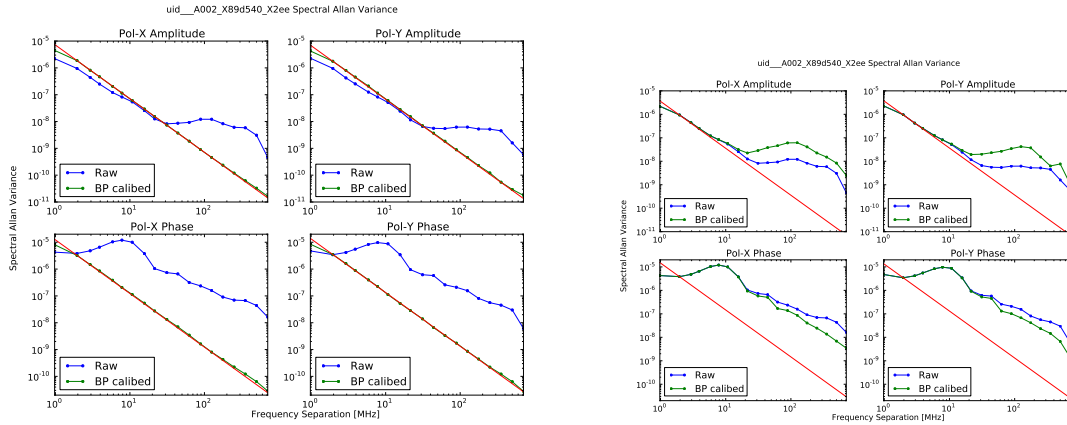


Figure 20: Spectral Allan variances of bandpass shape. Green and blue lines stand for the SAV before and after bandpass calibration, respectively. (Left): BP table was generated using the same FDM SPW. (Right): BP table was generated using the TDM SPW that covers the bandwidth of the target FDM SPW.

5 Discussion

The results in section 4 showed that the antenna-based bandpass stability performance was partially compliant at Band 3, 4, and 6 for limited cases and non-compliant for others. We quest for the origins of bandpass instability in this section and attempt to find the remedy for them.

5.1 Origins of bandpass variation

Finding origins of bandpass variation is crucial to control the bandpass stability. We give four candidates of control variables, random noise, elapsed time, sec Z difference, and azimuth difference to explain the bandpass variation as the dependent variable.

The random noise, S , is inversely proportional to the signal-to-noise ratio of visibilities. Since we apply bandpass calibration to the cross power spectra toward target sources, S is given by the RSS (root sum square) of random noise in the bandpass table and that in the target spectrum as

$$S^2 = \frac{1}{(N_{\text{ant,BP}} - 2)|V_{\text{BP}}|^2\Delta\nu T_{\text{BP}}} + \frac{1}{(N_{\text{ant,tg}} - 2)|V_{\text{tg}}|^2\Delta\nu T_{\text{tg}}}. \quad (13)$$

Here, N_{ant} is the number of antennas, V_{BP} and V_{tg} are visibilities of BP calibrator and target sources, and T_{BP} and T_{tg} are integration periods, respectively. The elapsed time, T , is the time difference between BP calibration and target scans. It relates to time variability of the bandpass shape. $\Delta \text{sec } Z$ and ΔAZ are the differences of airmass and azimuth angle between BP calibration and target scan, respectively.

We applied linear regression of the bandpass variation, ΔB , using multiple control variables of S , T , $\Delta \text{sec } Z$, and ΔAZ , as

$$\Delta B \sim a_0 + a_1 S + bT + c\Delta \text{sec } Z + d\Delta \text{AZ}, \quad (14)$$

where a_0 , a_1 , b , c , and d are coefficients for each control variable. We tried four indicators of the bandpass variation; SD and PE of amplitudes and phases.

Tables 2, 3, 4, and 5 lists the coefficients determined by the liner regressions to the indicators of the bandpass variation, SD of amplitude, PE of amplitude, SD of phase, and PE of phase, respectively. The numbers colored black, green, and yellow stand for the statistical significance with $P \leq 0.01$ (significant), $0.01 < P \leq 0.05$ (possible), and $P > 0.05$ (non-significant), respectively.

The random noise, related with a_0 , is always the primary control parameter for amplitude of bandpass variation, and also phase except Band 6. It is remarkable that the coefficient a_0 in SD amplitude lies in $a_0 = 0.39 \pm 0.06$ for TDM. This suggests that the bandpass error is predictable by giving the magnitude of random error, and allows us to design an optimal bandpass calibration procedure that fulfills desired bandpass accuracy. The coefficient for FDM is $\times 1.4$ as great as that for TDM. This possibly relates to the re-quantization loss in the FDM [Comoretto (2008)].

The secondary major component to explain the bandpass variation is the intercept, a_0 , which is independent of control parameters listed above. The magnitude of a_0 becomes greater at higher frequency bands.

Elapsed time, T , significantly relates to amplitude variation at Band 6 and phase variation at Band 3, 6, and 7. Since we did not measure long-term (> 1 day) stability at Band 4, 8, and

Table 2: Linear Regression of SD amplitude

Band	$a_0 (\times 10^{-3})$	a_1	$b (10^{-9} \text{ s}^{-1})$	$c (10^{-4})$	$d (10^{-4})$	R^2
3	0.47 ± 0.04	0.36 ± 0.01	-0.02 ± 0.01	8.04 ± 0.34	0.04 ± 0.01	0.92
4	0.79 ± 0.38	0.48 ± 0.04	-104 ± 115	23.1 ± 15.5	-7.02 ± 6.19	0.82
4 (FDM)	0.83 ± 0.18	0.56 ± 0.01	-61.8 ± 53.5	4.65 ± 7.19	-0.64 ± 2.87	1.00
6	0.96 ± 0.13	0.30 ± 0.05	3.07 ± 0.17	14.5 ± 0.58	0.80 ± 0.28	0.99
7	2.20 ± 0.35	0.38 ± 0.07	-2.38 ± 1.99	87.1 ± 38.2	-5.04 ± 2.75	0.99
8	3.74 ± 0.36	0.38 ± 0.02	377 ± 184	164 ± 127	-14.8 ± 16.2	1.00
9	5.81 ± 0.85	0.45 ± 0.03	-0.01 ± 0.24	-3.99 ± 20.7	-24.5 ± 39.9	0.99
10	6.44 ± 9.87	0.41 ± 0.02	11800 ± 31200	-690 ± 5320	-329 ± 1260	0.95

Table 3: Linear Regression of PE amplitude

Band	$a_0 (\times 10^{-3})$	a_1	$b (10^{-9} \text{ s}^{-1})$	$c (10^{-4})$	$d (10^{-4})$	R^2
3	1.19 ± 0.12	1.03 ± 0.03	-0.10 ± 0.03	19.52 ± 0.10	1.06 ± 0.35	0.91
4	2.08 ± 1.10	1.34 ± 0.13	-252 ± 334	49.6 ± 45.0	-16.4 ± 18.0	0.81
4 (FDM)	3.44 ± 0.81	2.02 ± 0.02	-247 ± 246	29.2 ± 33.1	-7.42 ± 13.2	1.00
6	1.78 ± 0.45	1.11 ± 0.17	7.60 ± 0.60	35.0 ± 0.20	2.17 ± 0.96	0.98
7	5.90 ± 0.96	1.04 ± 0.02	-3.39 ± 5.40	197 ± 104	-13.9 ± 7.45	0.99
8	9.21 ± 0.86	1.07 ± 0.04	1270 ± 433	500 ± 300	-54.9 ± 38.2	1.00
9	19.9 ± 3.51	1.06 ± 0.13	-0.18 ± 1.00	62.1 ± 85.3	-45.9 ± 164	0.98
10	39.7 ± 31.0	1.12 ± 0.06	-32500 ± 98000	9600 ± 16700	-1530 ± 3960	0.95

Table 4: Linear Regression of SD Phase

Band	$a_0 (\times 10^{-3})$	a_1	$b (10^{-9} \text{ s}^{-1})$	$c (10^{-4})$	$d (10^{-4})$	R^2
3	1.31 ± 0.12	0.32 ± 0.03	0.70 ± 0.03	4.46 ± 1.01	4.37 ± 0.35	0.87
4	1.09 ± 0.51	0.62 ± 0.06	-87.2 ± 157	16.0 ± 21.1	-7.24 ± 8.34	0.80
4 (FDM)	12.7 ± 0.27	0.54 ± 0.01	156 ± 83	-9.52 ± 11.1	-8.39 ± 4.44	1.00
6	2.35 ± 0.35	0.11 ± 0.13	2.96 ± 0.47	15.4 ± 1.57	-0.00 ± 0.07	0.90
7	2.94 ± 0.44	0.51 ± 0.01	-7.77 ± 2.51	78.9 ± 48.0	-4.09 ± 3.46	0.99
8	5.28 ± 0.48	0.51 ± 0.02	187 ± 244	43.4 ± 16.9	10.5 ± 21.5	1.00
9	10.2 ± 2.02	0.55 ± 0.08	1.09 ± 0.58	43.3 ± 49.2	-181 ± 94.7	0.97
10	371 ± 117	0.20 ± 0.02	-67700 ± 37000	9180 ± 6320	890 ± 1490	0.78

Table 5: Linear Regression of PE Phase

Band	$a_0 (\times 10^{-3})$	a_1	$b (10^{-9} \text{ s}^{-1})$	$c (10^{-4})$	$d (10^{-4})$	R^2
3	3.10 ± 0.32	1.00 ± 0.07	1.17 ± 0.7	13.90 ± 0.27	10.0 ± 0.92	0.83
4	3.41 ± 1.68	1.69 ± 0.20	-365 ± 517	60.3 ± 68.9	-27.3 ± 27.5	0.73
4 (FDM)	46.6 ± 0.87	1.98 ± 0.02	282 ± 265	2.88 ± 35.7	-38.8 ± 14.3	0.73
6	5.53 ± 0.93	0.56 ± 0.34	-6.29 ± 0.24	37.4 ± 0.41	-0.02 ± 1.97	1.00
7	8.07 ± 1.27	1.37 ± 0.03	-22.5 ± 7.2	251 ± 138	-16.1 ± 9.93	0.99
8	15.0 ± 1.22	1.33 ± 0.05	1180 ± 613	814 ± 424	-86.1 ± 54.0	1.00
9	33.8 ± 4.67	1.22 ± 0.17	2.17 ± 1.33	156 ± 113	-277 ± 218	0.98
10	1207 ± 344	0.43 ± 0.07	-248000 ± 10900	26200 ± 18600	5570 ± 4390	0.72

10, we could not obtain enough accuracy to determine the time dependence, b , at these bands. Although we had > 1 day span at Band 9, dependence on b was hidden behind random noise. Dependence on $\Delta \text{sec } Z$ was significant at only Band 3 and 6.

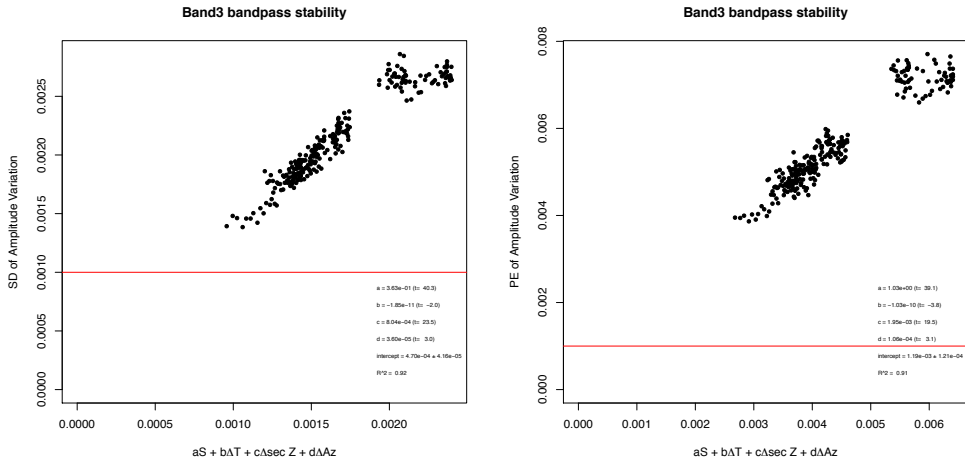
The adjusted R^2 values are greater than 0.9 for most of regressions. This means that the control parameters of S , T , $\Delta \text{sec } Z$, and ΔAZ explain the majority of bandpass variation. In other words, we can predict expected bandpass variations giving these control parameters.

5.2 Prediction of bandpass variation

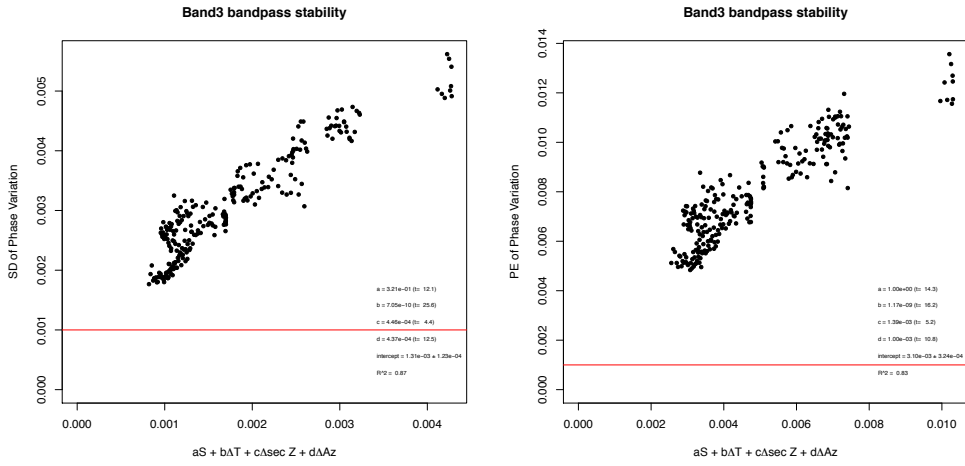
Using the linear regression coefficients and control parameters, we attempt to predict the bandpass variation. Figures 21 – 28 plots the bandpass variations with four different indicators (SD of amplitude, PE of amplitude, SD of phase, and PE of phase) as a function of the combination of control parameters weighted by coefficients. The red horizontal line indicates the required stability level of -30 dB.

The intercept corresponds to the minimal bandpass variation where control parameters are zero (i.e., infinite signal-to-noise ratio without T , $\Delta \text{sec } Z$ and ΔAZ). Since the intercept values of SD amplitude At Band 3, 4, and 6 are smaller than the requirement, relevant strategy of bandpass calibration allows us to fulfill the requirement. However, we have no chance to achieve the required stability at higher frequency than Band 7 where the intercept is greater than the goal.

Band 3



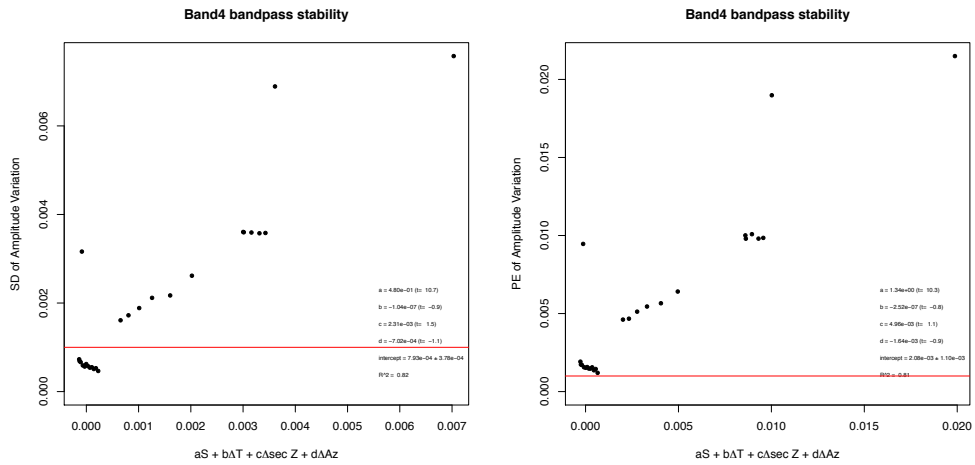
(a) SD (left) and PE (right) of bandpass amplitude variation at Band 3



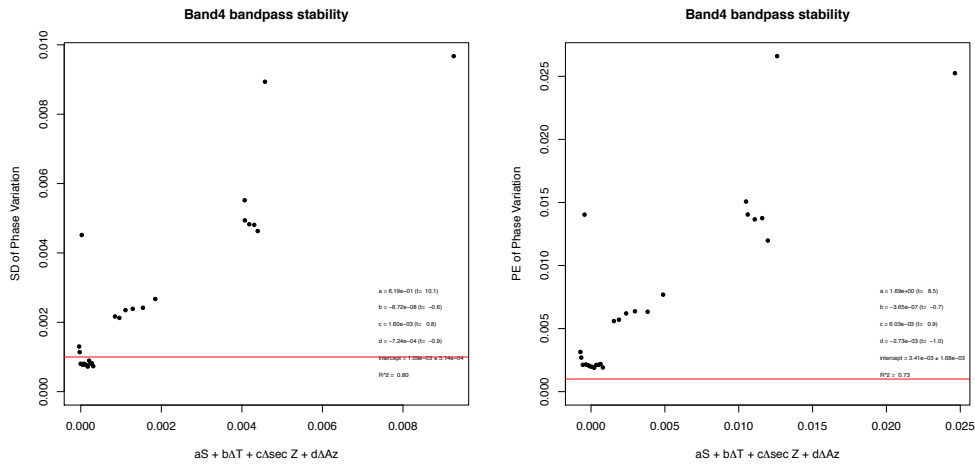
(b) SD (left) and PE (right) of bandpass phase variation at Band 3

Figure 21: Predicted and measured bandpass variations in Band 3. The red horizontal line indicates the required stability of -30 dB.

Band 4



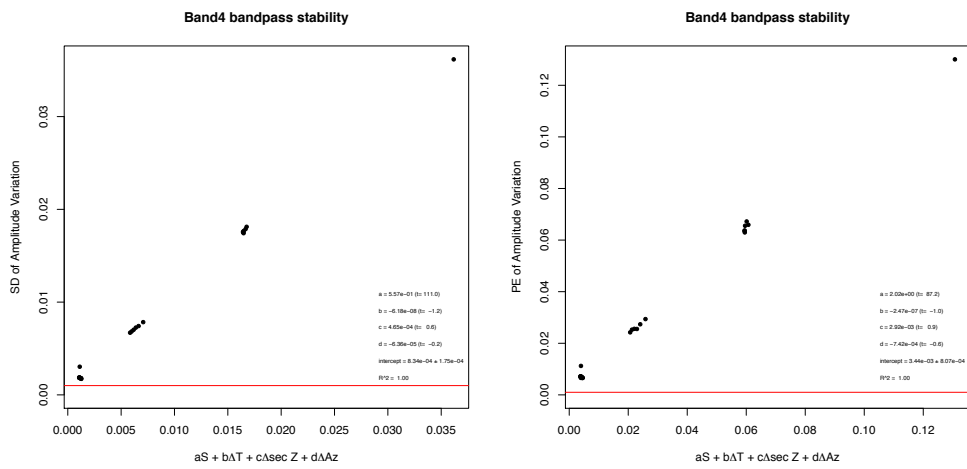
(a) SD (left) and PE (right) of bandpass amplitude variation at Band 4



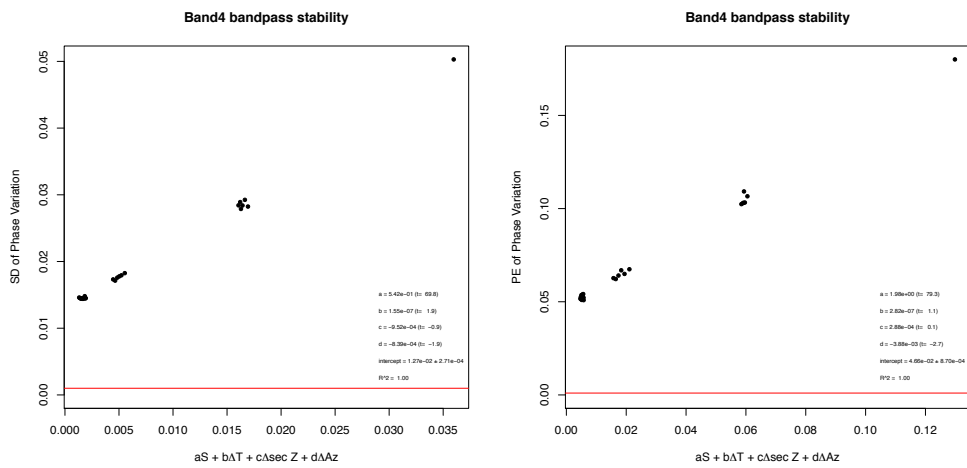
(b) SD (left) and PE (right) of bandpass phase variation at Band 4

Figure 22: Predicted and measured bandpass variations in Band 4

Band 4 (FDM)



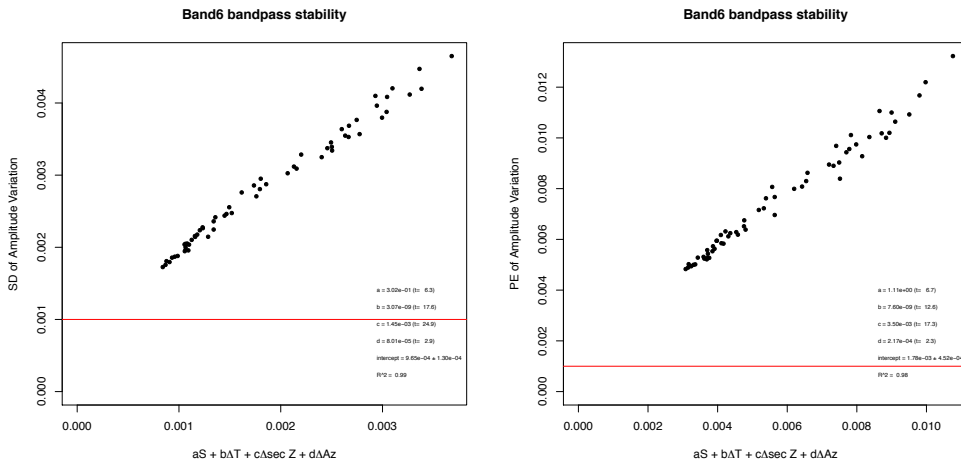
(a) SD (left) and PE (right) of bandpass amplitude variation at Band 4 FDM



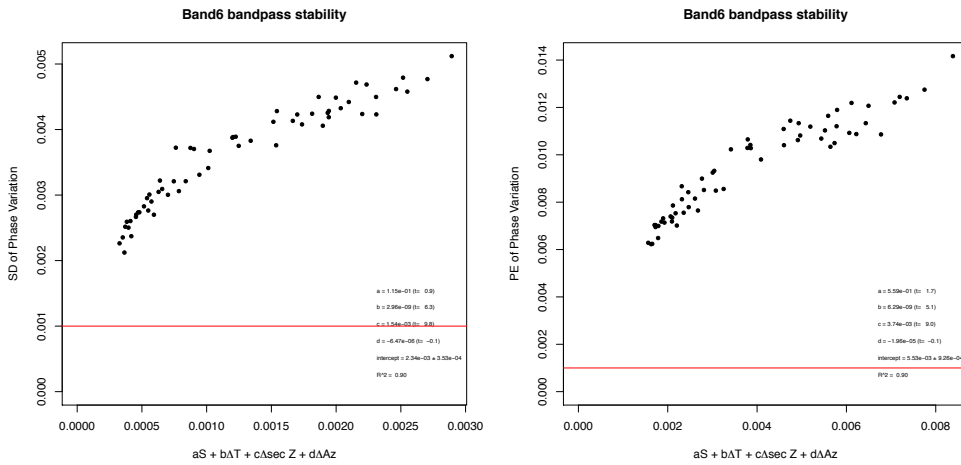
(b) SD (left) and PE (right) of bandpass phase variation at Band 4 FDM

Figure 23: Predicted and measured bandpass variations in Band 4 FDM SPW

Band 6



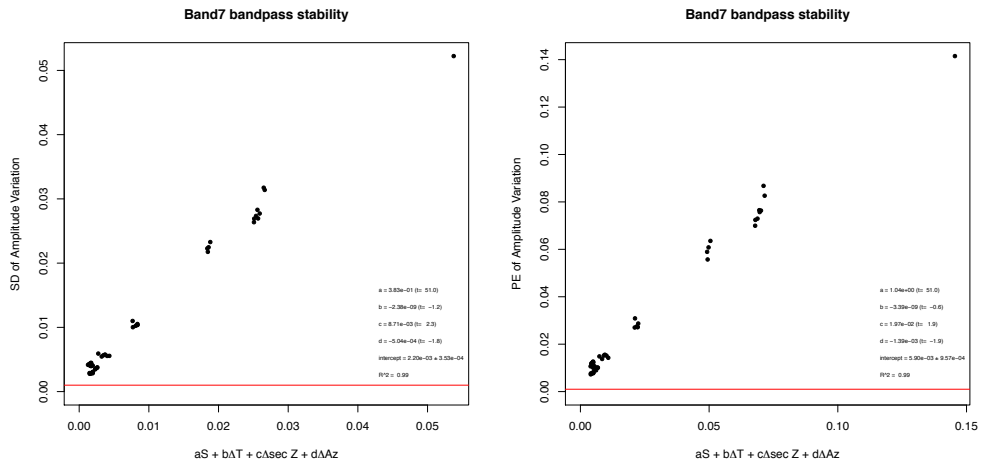
(a) SD (left) and PE (right) of bandpass amplitude variation at Band 6



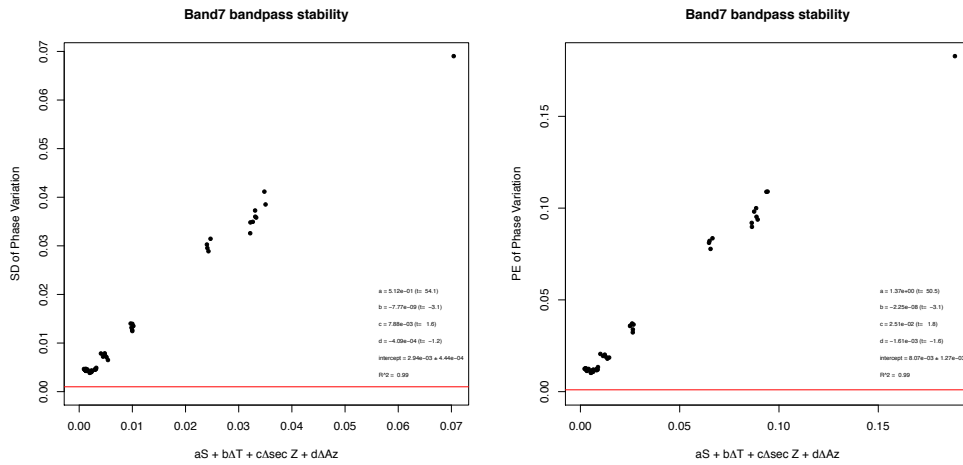
(b) SD (left) and PE (right) of bandpass phase variation at Band 6

Figure 24: Predicted and measured bandpass variations in Band 6

Band 7



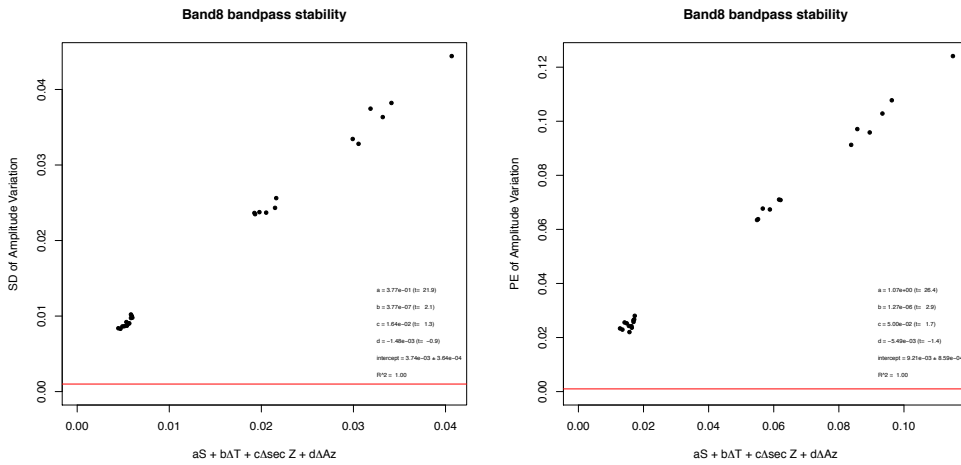
(a) SD (left) and PE (right) of bandpass amplitude variation at Band 7



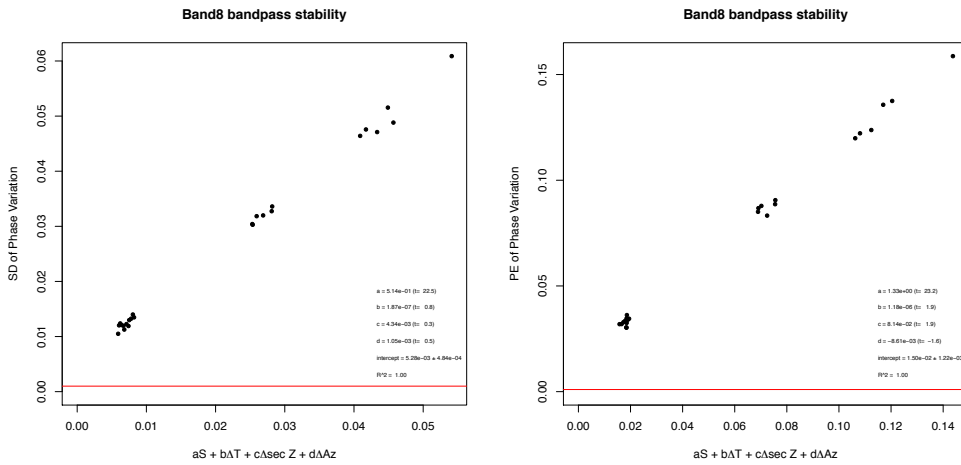
(b) SD (left) and PE (right) of bandpass phase variation at Band 7

Figure 25: Predicted and measured bandpass variations in Band 7

Band 8



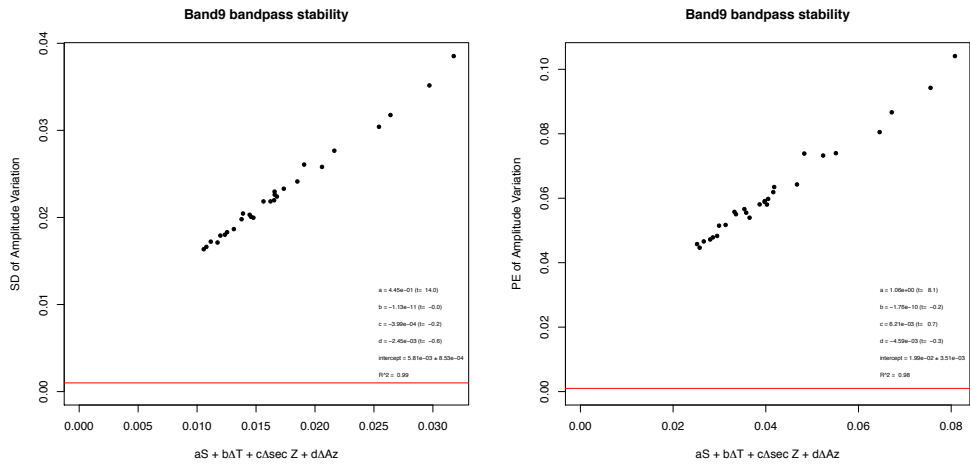
(a) SD (left) and PE (right) of bandpass amplitude variation at Band 8



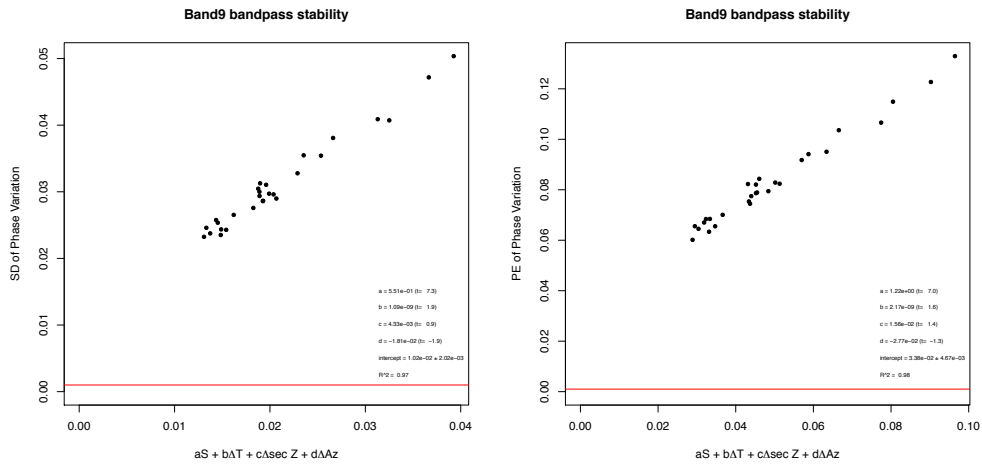
(b) SD (left) and PE (right) of bandpass phase variation at Band 8

Figure 26: Predicted and measured bandpass variations in Band 8

Band 9



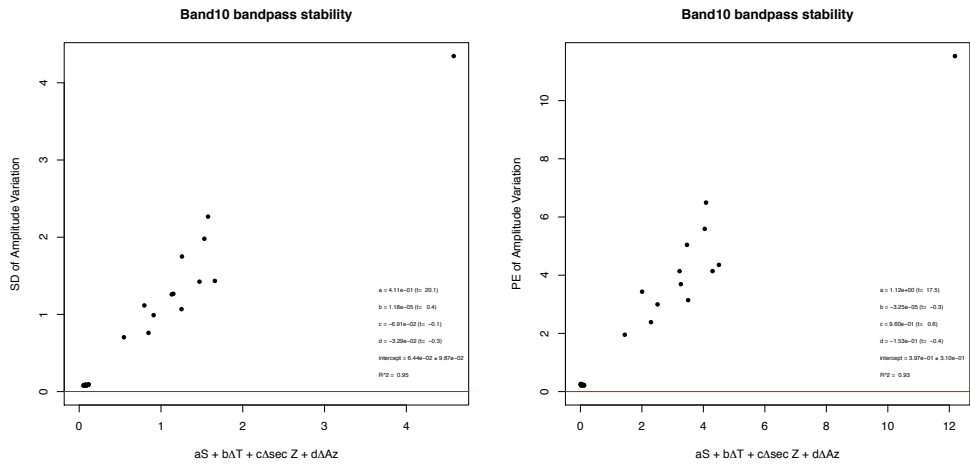
(a) SD (left) and PE (right) of bandpass amplitude variation at Band 9



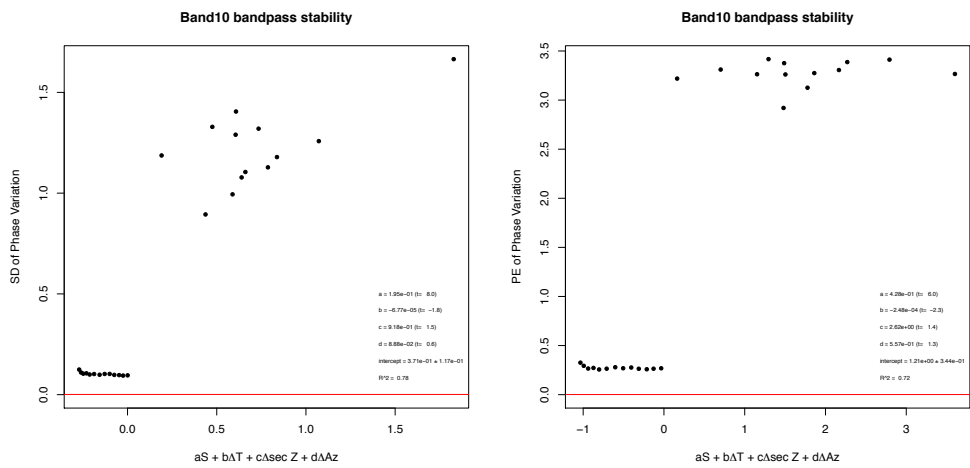
(b) Predicted and measured bandpass variations in Band 9

Figure 27: Predicted and measured bandpass variations in Band 9

Band 10



(a) SD (left) and PE (right) of bandpass amplitude variation at Band 10



(b) Predicted and measured bandpass variations in Band 10

Figure 28: Predicted and measured bandpass variations in Band 10

5.3 Bandpass flatness

As shown in the SAVs, the bandpass shape after bandpass calibration is flat for the frequency separation of $\Delta\nu < 100$ MHz, compared with the random noise. This indicates that Smoothed Bandpass Calibration [Yamaki et al.(2012)] will work to reduce the random noise in the bandpass table by smoothing with the frequency scale < 100 MHz. At higher frequency than Band 7, the bandpass undulation becomes less significant compared with the random noise and thus SBC will be more efficient to reduce the random noise that is the major component of bandpass variation.

Note that SBC should be applied only for the BP table and keep the spectral resolution toward target sources as desired.

5.4 Time instability of bandpass shape

The dependence of bandpass variation on T , denoted as b in the linear regression, is significant at Band 3 and 6. The amplitude dependence at Band 8 seems ridiculous because the short time span of observations (~ 1.5 hour) and non-significant dependence in SD amplitude. At other frequency bands, the detectability for b is not enough because of insufficient time span or signal-to-noise ratio.

The amplitude and phase dependence on elapsed time is less than $b < 10^{-8} \text{ s}^{-1}$ which will introduce amplitude variation of < -30 dB at $T = 1$ day. Thus, the bandpass shape is time-stable so that we can employ the of BP table obtained the day before the observation of target sources.

5.5 Az and El dependence of bandpass stability

Bandpass variation significantly relate to $\Delta \sec Z$ at Band 3 and 6, with the coefficient of $c 4 \times 10^{-3}$ at Band 6 and $c 2 \times 10^{-3}$ at Band 3. These results indicate that the bandpass calibration should taken near the target source ($\Delta \sec Z < 0.25$ and $\Delta \sec Z < 0.5$ for Band 6 and 3, respectively) to suppress the bandpass variation less than -30 dB.

Azimuth dependence is significant at only Band 3. This is probably relate to the influence of geomagnetism (FENCR-582).

We did not find significant ΔAZ and $\Delta \sec Z$ dependences of the bandpass variation at other frequency bands because of narrow azimuth or elevation coverage of the observations, or due to insufficient signal-to-noise ratio to detect them.

5.6 TDM-to-FDM bandpass transfer

The results presented in subsection 4.4 clearly suggest that a BP table generated in the TDM mode is significantly different ($\sim 2\%$) from that in the FDM mode. The TDM-to-FDM bandpass transfer will bring serious systematic errors in bandpass shape.

The different bandpass characteristics between TDM and FDM can caused by quantization loss and non-linearity through signal processing in the FDM.

Instead of employing TDM bandpass for FDM, SBC is an alternative to improve accuracy in the BP table. The SAV in the raw FDM BP table showed that the amplitude is flat at the frequency separation of $\Delta\nu < 31$ MHz. Thus, SBC with the smoothing window of ~ 30 MHz will work to reduce the random noise keeping undulation of the bandpass shape.

6 Summary

We verified the cross-correlation bandpass stability at Band 3, 4, 6, 7, 8, 9, and 10 using arrays with 21–35 antennas toward bright and compact continuum radio sources. Antenna-based bandpass tables with real-imaginary solutions showed slightly better accuracy than amplitude-phase solutions. The required bandpass stability of -30 dB in 1 hour was partially compliant at Band 3, 4, and 6, while bandpass variation exceeded the requirement.

The primary component of bandpass variation is the random (thermal) noise that relates to the signal-to-noise ratio. The secondary component is the intercept that becomes greater at higher frequency bands. The origin of the intercept is unknown. Elapsed time from BP calibration scan is a minor part to explain the bandpass variation. The BP table taken 1 day before will not bring systematic error greater than -30 dB. The atmospheric effect becomes comparable to the requirement when $\Delta \sec Z$ exceeds 0.25. Azimuth difference responses to the bandpass variation in only Band 3, probably due to geomagnetism.

The bandpass shapes in TDM and FDM are significantly different by $\sim 2\%$. Thus, TDM-to-FDM bandpass transfer will cause serious systematic error in bandpass calibrations. The FDM bandpass shape is flat enough in the frequency separation of $\Delta\nu < 31$ MHz and SBC will work to improve the accuracy of FDM BP table.

References

- [Bart et al.(1986)] Bart, E. E., Cohen, R. J., Davies, R. D., Rowland, P. R., & Norris, R. P. 1986, MNRAS, 219, 145
- [Comoretto (2008)] Comoretto G. 2008, ALMA memo 583
- [Yamaki et al.(2012)] Yamaki, H., Kamenno, S., Beppu, H., Mizuno, I., & Imai, H. 2012, PASJ, 64, 118